Probabilistic Resident Space Object Detection Using Archival THEMIS Fluxgate Magnetometer Data

Julian Brew[1]

The Guggenheim School of Aerospace Engineering, Georgia Institute of Technology, Atlanta, GA 30332

Marcus J. Holzinger[2]

The Guggenheim School of Aerospace Engineering, Georgia Institute of Technology, Atlanta, GA 30332

Abstract

Although the detection of Earth-orbiting space objects is generally achieved using optical and radar measurements, these methods are limited in the capability of detecting small space objects at geosynchronous altitudes. This paper examines the use of magnetometers to detect plausible flyby encounters with charged space objects using a matched filter signal existence binary hypothesis test approach on archival fluxgate magnetometer data from the NASA THEMIS mission. Relevant data-set processing and reduction is discussed in detail. Using the proposed methodology, 285 plausible detections are claimed and several are reviewed in detail.

Keywords: resident space objects; matched filter; admissible region; geostationary orbit; binary hypothesis testing

1. Introduction

As highlighted in the 2010 U.S. National Space Policy, the growing space debris problem is creating a major challenge for Space Situational Awareness (SSA) and the safe operation of government and commercial space assets [3]. The objective of Space Situational Awareness is to detect, characterize, and

[1]Graduate Research Assistant, NSTRF Fellow
[2]Assistant Professor

track Resident Space Objects (RSO). RSOs is then the plural. As of January 2016, the on-orbit catalogued RSO population was 17,260 objects greater than 10 cm [20, 5]. However, optical telescope data, radar station data, and spacecraft surface examinations suggest there are more than 100,000 objects between 1 and 10 cm and millions of objects smaller than 1 cm in orbit [26]. Although many space objects may be small (less than 1 cm), they pose a large threat to current and future operational space assets because of the high conjunction speed between objects in Earth orbit [36].

Presently, the U.S. Strategic Command Joint Space Operations Center (JSpOC) uses optical and radar measurements as the primary method in the detection of space objects [4]. However, in geosynchronous (GEO) orbits, where a large number of communications and weather spacecraft are located, optical and radar methods struggle at detecting small, faint objects [26]. With the accumulation of small debris in GEO orbits due to the fragmentation of retired satellites (see for example [12]), a method of detecting and characterizing small and poorly characterized space objects, in particular high-area-to-mass-ratio (HAMR) objects, is needed. The quantities, types, sizes, and orbits of debris in and around geostationary orbits are relatively unknown, outside of objects that are consistently bright and relatively unperturbed by solar radiation pressure, charge interactions with the magnetosphere, and other phenomena [14, 29, 30].

One possible detection method that addresses these needs is measuring induced magnetic fields generated by charged space objects as they pass near a magnetometer [19]. Due to presence of charged particles in the Earth's magnetosphere, RSOs in Earth orbit accumulate static Coulomb charges over time [31]. Because moving charged particles generate an electromagnetic field, magnetometers can in theory sense these phenomena and can be used to detect, track, and characterize charged space objects [19]. This concept has been pursued in Low Earth Orbit (LEO) experiments such as Clementine (orbital meteoroid and debris counter) [21], although to limited effect. Capacitor detectors that sensed magnetic field fluctuations above a specified threshold were used; this resulted in statistical space debris representations. A flyby encounter detected by a magnetometer differs as it provides a sequence of three axis magnetic field measurements as a function of time for each RSO encounter. Additionally, charge screening at LEO altitudes limited the capacitive detection range to the order of meters.

Unfortunately, an encounter between a magnetometer with a known orbit and a charged RSO flyby does not yield a full orbit solution; there are a

number of observable and unobservable dynamics parameters for encounters between a charged RSO and a three axis magnetometer. Previous investigations have shown the orientations of the charged object flyby within the encounter plane and the closest approach distance cannot be determined with the given magnetic encounter information [19]. However, hypothesized constraints based on the RSO orbit energy, periapsis radius, Coulomb charge, and the detection range of the sensing magnetometer can be imposed to identify admissible regions for initial orbit determination efforts [24, 35]. This is analogous to the admissible region approach for initial orbit determination described by [24] for optical systems but using a different phenomenology.

A detection technique is needed to identify the expected magnetic field signature of a charged particle flyby within magnetometer data. Matched filters are formed by correlating a known template signal with the unknown signal to detect the presence of the known signal in the unknown signal [18]. With additive stochastic noise, matched filters maximize the flyby signature signal to noise ratio (SNR) gain [37]. Using the Biot-Savart law [34], induced magnetic field template signals can be generated that depend on the relative motion between the magnetometer and the space object. These template signals can be used in conjunction with matched filters to detect the presence of a magnetic field signature characteristic of a charged RSO flyby in experimental data. To rigorously test the signal existence hypothesis against evidence contained in the empirical signal, binary hypothesis tests are conducted [25, 22]. Additionally, being able to specify a rate of false detections and a threshold on signal existence probability to result in a hypothesized detection adds substantial rigor to the process. This approach is very similar to track-before-detect methods for detecting space objects using optical systems. In track-before-detect methods, a sequence of image frames are taken and the direction and velocity of a space object are hypothesized. Then statistical evidence is found to support that object's existence by evaluating the goodness of each track [27].

In this paper, the banks of matched filter hypotheses are applied to fluxgate magnetometer data acquired from the NASA "Time History of Events and Macroscale Interactions during Substorms" (THEMIS) mission [7, 6].

Matched filters perform convolutions between the known template signal and the unknown signal [37]. While a time convolution is usually the correlation method used in matched filters, a different variation of the matched filter using Pearson product-moment correlation coefficient [13] is presented in this paper. In this paper, a matched filter scoring method is introduced

and shown to approximate the SNR of the magnetic field fluctuation due to the charged RSO flyby.

The contributions in this effort include: 1) the generation of Matched Filter template hypotheses is described 2) a signal existence hypothesis test framework is developed and explained and 3) an examination of archival on-orbit THEMIS data is performed to identify plausible RSO detections. and 4) spatial / temporal analysis of plausible detections, consistency with geostationary objects, and relevant space weather.

2. Theory

2.1. Expected Magnetic Signatures of RSO Flyby

Earth orbiting objects interact with the space plasma environment, resulting in the accumulation and transport of electric charge. Because of this, spacecraft and space objects can acquire a static Coulomb charge over time. Low altitude orbiting spacecraft (LEO) usually experience less charging effects than at high altitude (GEO), where the spacecraft encounter high-energy, low-density electrons [9]. Freuh et al. used numerical simulation of the magnetic field and solar wind activity to estimate the Coulomb charges of space debris material, in particular mylar and kapton. For these materials, the total charge can range from -0.003 to -0.115 Coulombs in GEO depending on solar weather and material capacitance [8].

For charged RSO encounters, an approximate flyby motion model was derived by Holzinger [19]. In the flyby motion model, the local relative motion is approximately linear over the ranges at which the magnetic field can be detected. From the Biot-Savart law, the magnetic field $\boldsymbol{B}(t)$ sensed at the magnetometer location and generated by a moving object with sensed charge q_s (Coulombs), relative velocity $\dot{\boldsymbol{\rho}}$, and relative position $\boldsymbol{\rho}$ is

$$\boldsymbol{B}(t) = \left(\frac{\mu_0 q_s}{4\pi}\right)\frac{\dot{\boldsymbol{\rho}}(t)\times\boldsymbol{\rho}(t)}{\|\boldsymbol{\rho}(t)\|^3} \tag{1}$$

where $\boldsymbol{B}(t)$ is in units of Teslas, $\mu_0 = 4\pi \times 10^{-7}$ Vs/Am is the magnetic permeability, $\dot{\boldsymbol{\rho}}(t)$ has units of meters per second, and $\boldsymbol{\rho}(t)$ has units of meters. Rewriting Eq. (1) with assumed relative motion model, the final observable measurement equation for a magnetometer with a moving charged particle can be written as

$$\boldsymbol{B}(t) = -\left(\frac{\mu_0}{4\pi}\right)\frac{\mathcal{Q}_s\omega_m}{(1+\omega_m^2(t-t_c)^2)^{\frac{3}{2}}}\hat{\boldsymbol{p}}(\alpha,\beta) \tag{2}$$

where t_c is the time of closest approach and $\hat{\boldsymbol{p}}(\alpha, \beta) = \boldsymbol{\rho} \times \dot{\boldsymbol{\rho}} / \|\boldsymbol{\rho} \times \dot{\boldsymbol{\rho}}\|$ is the unit vector that defines the plane of motion of the encounter parametrized in polar coordinates α and β [19]. Both the distance normalized apparent charge parameter, $\mathcal{Q}_s = q_s/\rho_\perp$, and the maximum apparent angular rate $\omega_m = \|\dot{\boldsymbol{\rho}}\|/\rho_\perp$ have been normalized by the closest approach distance of the RSO to the magnetometer $\rho_\perp$. From this, there is an unobservable two-dimensional subspace with respect to $\rho_\perp$ and the orientation of the flyby in the encounter plane. For signature detection, however, it is only necessary to examine $\|\boldsymbol{B}(t)\|$. This reduces the number of unobservable parameters to one, $\rho_\perp$.

Depending on the sampling rate and corresponding Nyquist frequency of the sensing magnetometer, there are inherent limitations on the relative RSO speeds that the magnetometer can accurately detect. Conversely, depending on the expected relative speeds between the magnetometer and the RSO, there may be a limitation on the required magnetometer sampling rate to capture the RSO encounter.

Holzinger discussed the effect of charge screening and local space weather on the sensed magnetic field [19]. Due to the interaction between an orbiting object and the space plasma environment, the sensed charge of an object is reduced. Consequently, the sensed magnetic field due to this charge is also weakened. The Debye length, denoted by λ_d, is the characteristic distance parameter that describes the exponential decay of charge screening. At GEO altitudes, the effective Debye lengths of plasma are on the scale of 4 -1000 m enabling the detection of charged objects on the order of meters to hundreds of meters [31].

For the charged object to be detected by the magnetometer and distinguished amongst local variations in the magnetic field, the SNR of the induced magnetic field Eq. (2) must exceed a set threshold. Using this, the following detection constraint in Eq. (3) for a RSO detection using a magnetometer is created [19].

$$\rho_\perp^2 e^{\frac{\rho_\perp}{\bar{\lambda}_d}} \sigma SNR_{det} \leq \left(\frac{\mu_0 |q_v|}{4\pi}\right) \|\dot{\boldsymbol{\rho}}\| \tag{3}$$

The bounds of this inequality can be found analytically.

$$\rho_{\perp,max} = 2\bar{\lambda}_d W\left(\frac{\sqrt{\frac{\mu_0}{4\pi}|q_v|\|\dot{\boldsymbol{\rho}}\|}}{2\bar{\lambda}_d\sqrt{\sigma SNR_{det}}}\right) \tag{4}$$

W is Lambert W (also known as the product logarithm) function [11] and

is the analytical solution to $f(x) = xe^x$. Eqn. (4) gives the maximum closest approach distance for a magnetometer RSO detection as a function of the vacuum charge of the RSO (q_v), the relative velocity of the RSO to the magnetometer ($\|\dot{\boldsymbol{\rho}}\|$), the local space weather conditions given with the effective Debye length ($\bar{\lambda}_d$), and the measurement precision of the magnetometer (σ). For example, Figure 1 displays the RSO detection capability of the THEMIS fluxgate magnetometers at GEO altitudes and various effective Debye lengths. Stiles et al. computed the effective Debye lengths using the Debye-Huckel approximation during low, nominal, and high levels of solar activity [31].

Under the best-case conditions of space weather and charge, the THEMIS fluxgate magnetometers are able to detect RSO flyby signatures at a distance of about 650 m. Figure 1 shows the magnetometer detection capability under low, nominal, and high levels of solar activity [31]. It should be noted that this upper limit depends on the relative speed between the magnetometer and the charged objects. The THEMIS fluxgate magnetometers in consideration are capable of a sampling rate of 128 Hz. At this rate, the magnetometers can measure sufficient samples to capture RSO flyby encounters with relative speeds of about 2400 m/s. This is a conservative upper bound on the relative velocity based on the assumptions that the smallest measurement interval for a detection is 5 samples and the smallest closest approach distance $\rho_{\perp,min} = 25$ m. Although this speed can be relatively large for GEO altitude encounters, the maximum detection distance described in Eqn. (4) scales logarithmically with relative speed. For example, above 500 m/s, a decrease in the relative speed by a factor of two results in about an 11% decrease in the detection range defined by $\rho_\perp$.

2.2. Potential Magnetosphere Phenomenon

Natural magnetosphere phenomenon are of particular importance to the detection of RSOs through magnetometer flybys. It is necessary to avoid falsely attributing a variation in the magnetometer signal to the charged RSO phenomenon of interest. To avoid these false positives, all other magnetic field phenomena need to be considered. Depending on the frequency and magnitude of the extraneous magnetic field variations, it becomes more difficult to detect low SNR RSO signatures and to distinguish between the RSO signatures and local variations in the magnetic field. Furthermore, local magnetosphere phenomenon are time-varying and difficult to predict. Therefore, signal conditioning is required in the process of detecting charged RSO

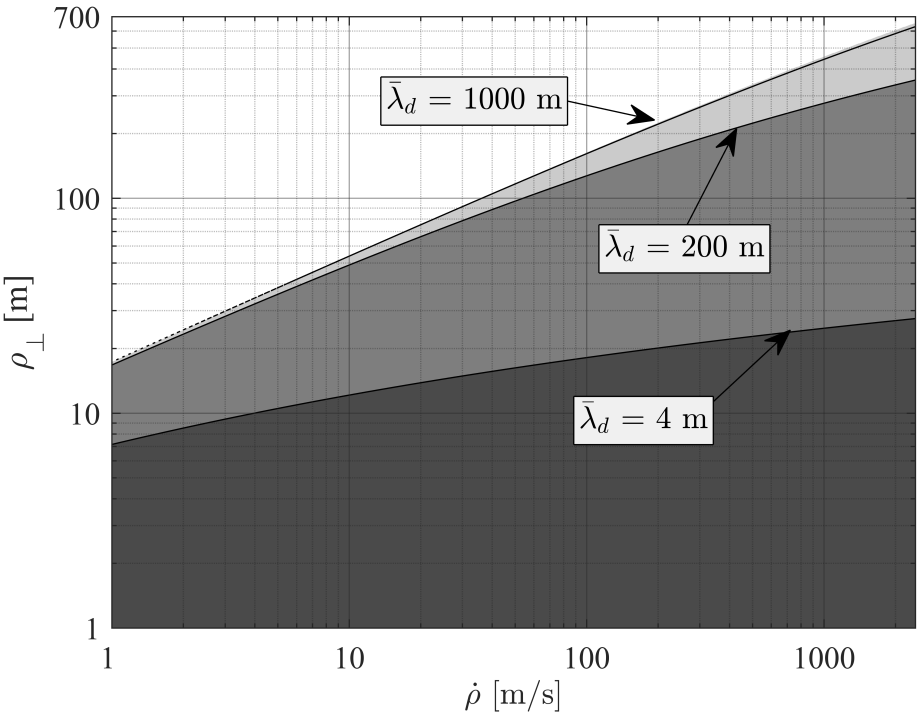

Figure 1: Detection capability of THEMIS magnetometer at various space weather conditions

encounters to attenuate the signals due to magnetosphere phenomenon.

The magnetosphere is the boundary that separates Earth's magnetic field and the solar wind. Inside of the magnetosphere the varying conditions, typically referred to as space weather, greatly depend on the solar activity. The interaction between the solar wind and the magnetosphere creates phenomena such as the bow shock, magnetopause, magnetotail, magnetic field reconfigurations, and geomagnetic storms [28, 39, 23].

The geomagnetic main field of the Earth is slowly varying and originates within the Earth. However, more rapid variations, with periods from seconds to days, are produced by the interaction between Earth's magnetic field and the Sun's radiation [28, 10]. For a spacecraft in orbit, the primary magnetic field of Earth as seen by the magnetometer varies periodically. However on the time scales of RSO flybys, these magnetic field variations are linearly varying with time.

There are two primary effects of the Sun due to it's position relative to the Earth - quiet day magnetic variations and magnetic storms. A quiet day magnetic variation originates from the Sun's electromagnetic and thermal radiation. As the day side of the Earth is illuminated and heated, the Sun's radiation heats the ionosphere causing convection. The convection moves charged particles through the Earth's magnetic field which itself produces a magnetic field that is fixed on the day side of the Earth. As a spacecraft in orbit passes over the day side of the Earth, it experiences these quiet day magnetic variations [28] creating a orbit periodic variation. Magnetic storms, on the other hand, are a product of the Sun's ejection of solar wind. Coronal mass ejections from the Sun's surface further compress the magnetosphere causing a sudden change in the magnetic field. At GEO altitudes, it can be shown that the local magnetic field variation is positively proportional to variations in solar wind dynamic pressure [38]. Because solar wind dynamic pressure is variable and unpredictable in time, the resulting magnetic field fluctuations vary stochastically and do not have stationary statistics. Additionally, due to geomagnetic storms and the Earth's magnetic bow shock, there may be occasional jump discontinuities in the magnetometer signal as the spacecraft passes between different regions of magnetic activity [39]. These magnetic field variations are analogous to step disturbances. Similar to the shape of a stair step, these disturbances occur when the magnetic field undergoes a discontinuous change instantaneously.

Another phenomenon of interest is geomagnetic pulsations, which are periodic plasma waves in the Earth's magnetosphere that can range from about 0.0016-10 Hz [17]. The higher frequency waves are proton ion-cyclotron waves in the magnetospheric plasma and can reach amplitudes of a few nanotesla [17]. An example of these pulsations in the THEMIS-D data can be seen in Figure 2. At the higher frequencies, these pulsations can significantly alter the frequency content of the local magnetic field. However, it is possible to distinguish between the geomagnetic pulsations from a charged RSO flyby signature by the number of cycles and the appropriate signal filtering.

2.3. Signal Conditioning

Only the induced magnetic field due to a RSO flyby is desired in the matched filter scoring process. In general, the baseline magnetic field can be approximated using numerical Earth magnetic field models such as the International Geomagnetic Reference Field (IGRF) [33] and the World Magnetic Model (WMM) [10]. However, there are model uncertainties on the

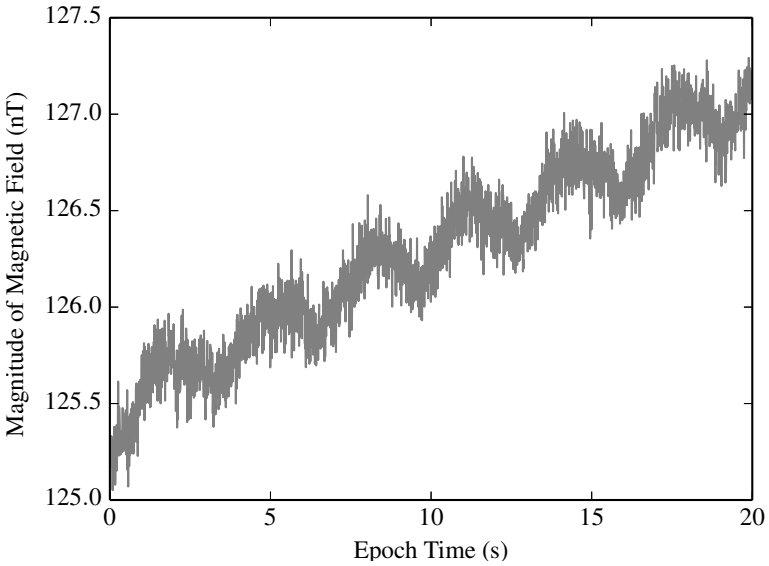

Figure 2: Geomagnetic pulsations in THEMIS-D data with epoch time of Wednesday, 09-Sep-15 07:00:08.434 UTC

order of 150 nT [10] and significant spatial variations in the Earth's magnetic field [23]. Additionally, the variations in the local magnetic field due to space weather phenomena must also be attenuated as much as possible for the matched filter.

Thus, the raw magnetometer data must be processed to locally approximate the baseline magnetic field. This can be achieved using digital signal processing methods described as a Laplace transform in Eq. (5), where $r(s)$ is the residual signal, $d(s)$ is the raw signal, and $L(s)$ is a zero-phase low pass Butterworth filter of the fourth order [32]. This filtering process is demonstrated in Figure 3. In this particular application of the low pass filter on a synthetic test signal, the cut-off frequency ($\omega_h = 50$ (rad/s)) was chosen to isolate the magnetic field spike at 50 seconds. Different cut-off frequencies can be chosen to isolate data at a desired frequency.

As will be discussed in the next section, the proposed detection method requires a hypothesized flyby rate and time of closest approach. For the application to magnetometer data, the cut-off frequency of the low pass filter, ω_c (rad/s) , is a function of the hypothesized flyby frequency ω_h (rad/s) to ensure that only frequencies substantially slower than the hypothesis fre-

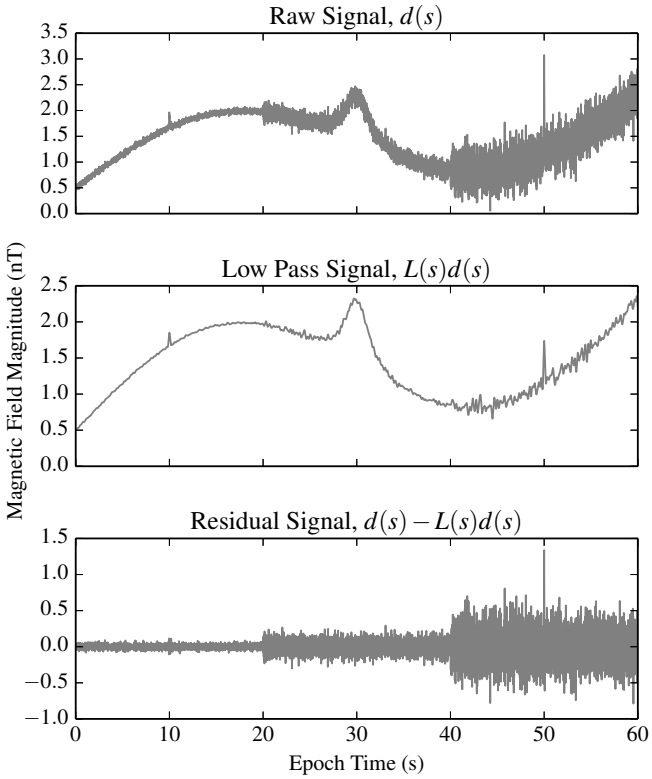

Figure 3: Demonstration of low pass filtering process for a synthetic test signal

quency are attenuated, leaving signals with frequency content relevant to the hypothesis, shown in Eq. (6). The choice of $k = 4\pi$ ensures the cutoff frequency is both sufficiently below the ω_h of interest to avoid signal attenuation at that frequency [32]. This results in isolating the zero-mean magnetic field signal that describes the local fluctuations at and above the frequency of interest ω_h.

$$r(s) = (1 - L(s, \omega_c))d(s) \tag{5}$$

$$\omega_c = \frac{\omega_h}{k} \tag{6}$$

2.4. Matched Filtering

A template (hypothesis) signal is created from the expected RSO flyby magnetic field signature described in Eq. (2). To avoid a template signal dependence on the charge q_s and the unobservable parameter $\rho_\perp$ the template signal used in the matched filters is shown in Eq. (7). This makes each template signal solely a function of ω_h and avoids any assumption on the charge of the object. Examples of the template signals with varied ω_h can be seen in Figure 4.

$$g(t;\omega_h) = \frac{\omega_h}{(1+\omega_h^2(t-t_c)^2)^{\frac{3}{2}}} = \frac{\|\boldsymbol{B}(t)\|}{(\frac{\mu_0}{4\pi})\mathcal{Q}_s} \tag{7}$$

The matched filters applied to the THEMIS magnetometer data use the Pearson product-moment correlation coefficient [13] when correlating the template signal and the magnetometer data signal.

$$\rho_{g,B} = \frac{\text{cov}(g,B)}{\sigma_g \sigma_B} \tag{8}$$

where $\text{cov}(g,B)$ denotes the covariance between the template signal and the magnetic field magnitude signal and σ_g, σ_B denote the standard deviation of the template and magnetic field magnitude signal.

The correlation coefficient metric is used because the magnitude of the typical, convolution-based matched filter score is also a function of ω_h. The correlation metric allows the binary hypothesis testing thresholds to be in terms of signal-to-noise ratio. However, this matched filter metric results in correlations valued between -1 and +1 for an purely negative and positive correlation, respectively. It is then convenient to scale these results based on the magnitude of the magnetic field fluctuations. As a result, the acquired correlation coefficients are scaled by the local SNR of the magnetometer signal to acquire an approximate flyby SNR. The local SNR of the magnetometer signal is defined as

$$\text{SNR}^2(t) = \frac{\|\boldsymbol{B}(t)\|^2}{\sigma(t)^2} \tag{9}$$

where the magnetometer is assumed to have noise characterized by a zero-mean Gaussian and time varying standard deviation of $\sigma(t)$. Under this scaling metric defined in Eq. (9), the SNR of the RSO flyby magnetic field

signature is approached and low intensity magnetic field fluctuations do not affect the output of the matched filters. Note that the $B(t)$ described thus far is the induced magnetic field from the RSO flyby. This can be acquired by subtracting the baseline magnetic field from the raw magnetometer signal as discussed in Section 2.3.

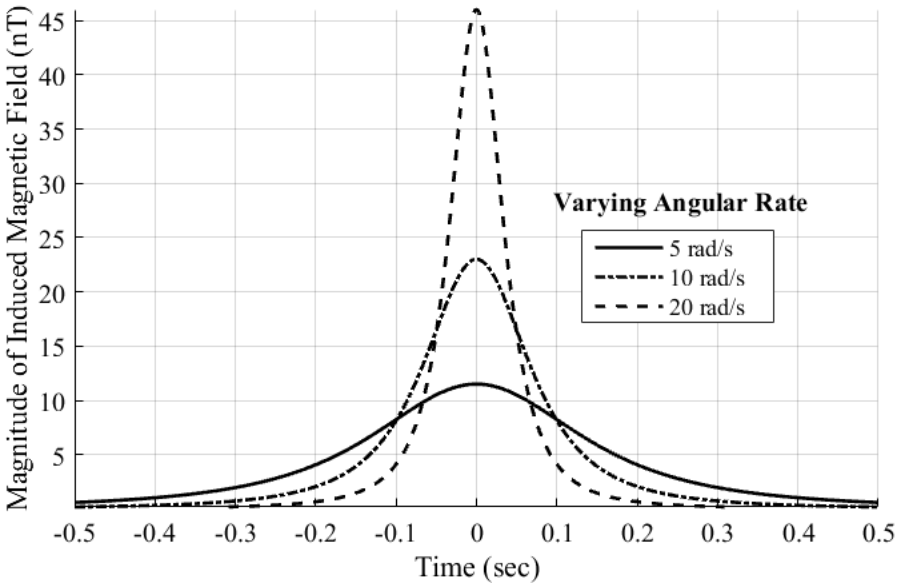

Figure 4: Example template signal with varying angular rate (ω_h)

As previously mentioned, matched filters are formed by correlating template and data signals through time. However, the induced magnetic field from the RSO flyby drastically changes with the relative flyby angular rate, ω_m. To effectively detect RSO encounters over a wide range of RSO flyby angular rates, the matched filter described above is applied to the magnetometer data signal multiple times with varying hypothesis flyby angular rates ω_h. This scoring process, illustrated in Figure 5, is defined as the application of the matched filters with varied template signals (defined by ω_h) . Now instead of a one-dimensional matched filter output signal, a two-dimensional scoring surface is generated as a function of hypothesized time of closest approach t_c and RSO flyby angular rate ω_h. Additionally, the scoring surface approximates the SNR of the hypothesized RSO flyby. Thus, a matched filter detection is defined as an approximate SNR, greater than a specified mini-

mum SNR threshold for a candidate RSO flyby ($SNR_{\text{MF}} > SNR_{\text{thresh}}$). Because the scoring surface is defined using the hypothesized time of closest approach and RSO flyby angular rate, the local maxima of the scoring surface correspond to the t_c and ω_h of the candidate RSO flyby.

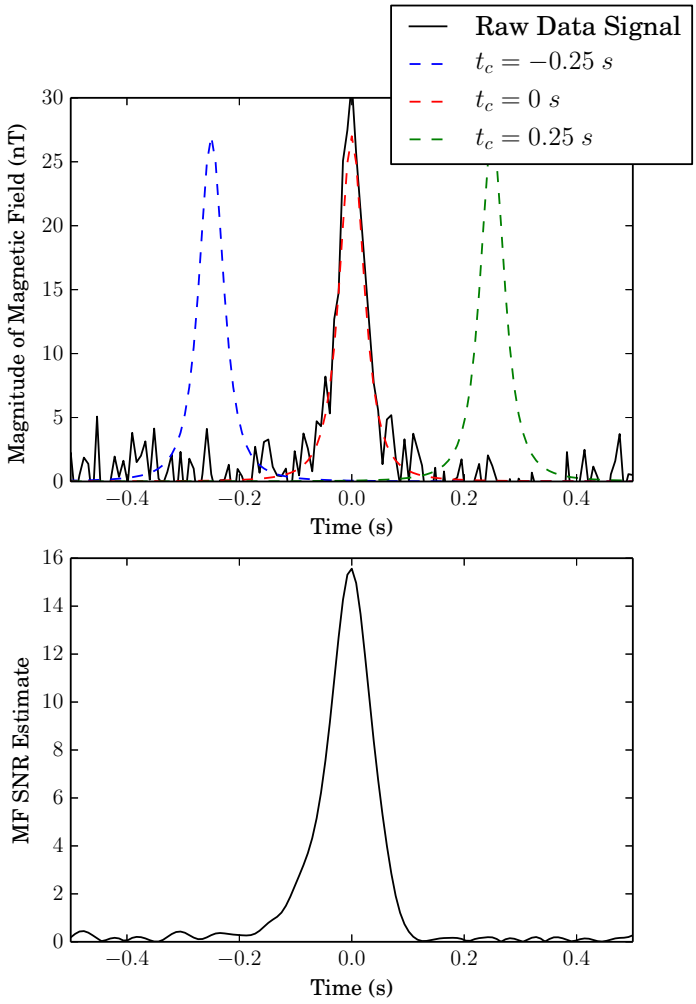

Figure 5: Visualization of Matched filter

By varying ω_h of each template signal in the scoring process, the time interval of the template signal is also being varied. If the scaling parameter $\alpha \in (0, 1)$ is defined, the duration of the hypothesis flyby can be quantified.

Using the geometry described in Figure 6 and the magnetic signature described in Eq. (2), the flyby duration can be calculated as shown in Eq. (10).

$$\Delta t = 2\frac{\sqrt{\alpha^{-2/3}-1}}{\omega_m} \tag{10}$$

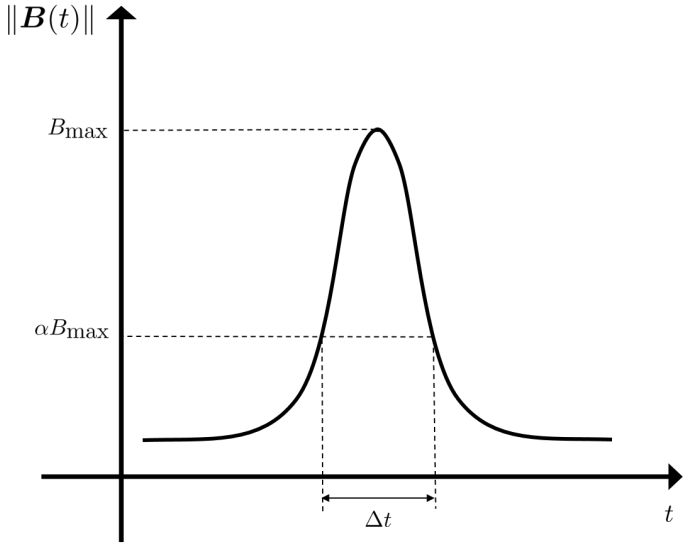

Figure 6: α parameter geometry

The chosen value of α can vary depending on the sampling rate of the magnetometer data and the range of ω_h used in the matched filter scoring process. For example, the minimum time interval may be defined such that there are a minimum of 5 samples measured. At a sampling rate of 128 Hz, this corresponds to a minimum time interval of about 39 milliseconds. An additional constraint on the maximum value of ω_m can be enforced by selecting lower and upper bounds for $\rho_\perp$ and $\dot{\rho}$, respectively. A conservative estimate of the minimum expected closest approach distance of $\rho_{\perp,min} = 25$ m is chosen. Due to the 128 Hz maximum sampling rate of the THEMIS fluxgate magnetometers, the largest relative speed that can be detected in a magnetic field signature is $\dot{\rho}_{max} = 2430$ m/s. With constraints on both $\rho_\perp$ and $\dot{\rho}$, the required $\alpha \approx 0.0166$. By keeping α fixed during the scoring process, a given ω_h maps to a unique template function as shown in Eq. (10). This α parameter also ensures equal weighting between matched filter results over multiple ω_h.

Due to the inclusion of α, the template signals of the matched filter scoring process are defined over different durations. Consequently, the matched filter results incur time delays that depend on ω_h. Therefore, the hypothesized closest approach time (t_c) is $\Delta t/2$ after the initial template signal. All of the results of this paper include this time shift.

2.5. Feasible Charge Limitation

From Eq. (3) the possible vacuum charge can be found as a function of closest approach distance, $\rho_\perp$, given the estimated SNR and hypothesized ω_h from the scoring process. After assuming a Debye length $\bar{\lambda_d}$, it is possible to create a curve as shown in Figure 7. As a result of range limitations on both closest approach distance and vacuum charge, there is a limited solution space for plausible RSO flyby signatures. Graphically, only charge and distance solutions that lie within the unshaded region are feasible for the expected RSO signatures. As a result, the hypothesized RSO flyby for this particular SNR and ω_h would occur within a closest approach distance of about 185 m.

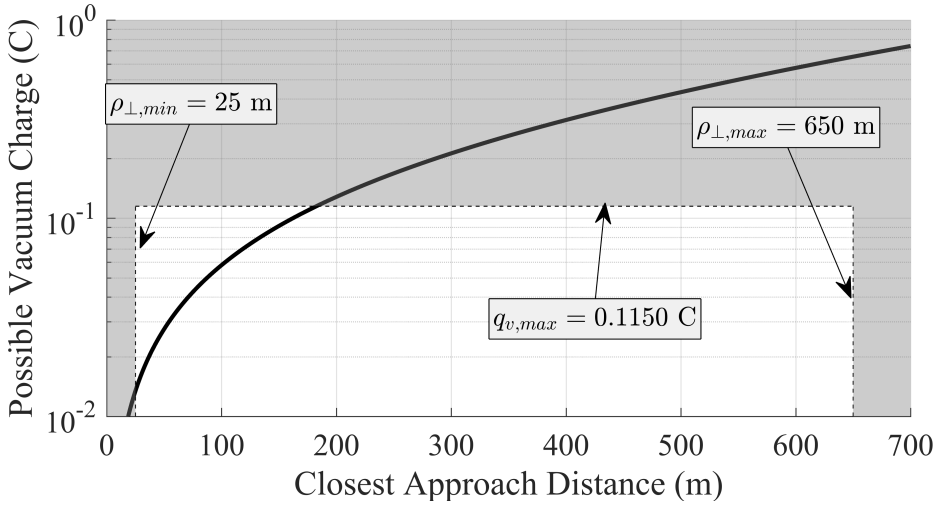

Figure 7: Potential static charge with varying closest approach distance (SNR = 5.7, ω_h = 1.6 rad/s, $\bar{\lambda_d}$ = 1000 m)

As the effective Debye length, $\bar{\lambda_d}$, is decreased, the slope of the charge distance curve increases. However, due to the exponential scale of the Debye length, decreasing the effective Debye length from a maximal value of $\bar{\lambda_d}$ =

1000 m to a nominal value of $\bar{\lambda_d} = 200$ m decreases the possible closest approach range from 185 m to 148 m (20% reduction). Additionally, the ratio $\sigma\text{SNR}/\omega_m$ is proportional to the slope of the charge distance curve. As a result, there is an upper limit of $\sigma\text{SNR}/\omega_m$ defined by the maximum possible vacuum charge, the minimum closest approach distance, and the effective Debye length. The upper limit of $\sigma\text{SNR}/\omega_m$ can be calculated analytically by rearranging Eq. (3).

$$\left[\frac{\sigma SNR}{\omega_m}\right]_{max} = \frac{\mu_0 |q_v|}{4\pi} |\mathcal{Q}_{v,max}| e^{-\frac{\rho_{\perp,min}}{\lambda_d}} \tag{11}$$

This upper limit of this ratio enforces an additional constraint on the SNR of the hypothesized RSO encounter. Graphically, this creates an upper boundary surface for scoring surfaces similar to Figure 13. Placing a conservative upper bound on the $\sigma\text{SNR}/\omega_m$ helps identify matched filter false positives by checking whether the signal of interest could have been by a charged RSO flyby.

2.6. Binary Hypothesis Testing

Matched filtering has known issues with incorrectly detecting the template signal within the data signal. Due to the aforementioned uncharacterized geomagnetic phenomenon, signals with substantive sustained non-zero mean signals are sometimes misidentified as a charged RSO flyby signature. The overall number of these false positives can be selected by the operator by using Binary Hypothesis Testing (BHT) [25, 22] on the results from the matched filtering procedure.

Hypothesis testing involves deciding whether an event occurs given a set of data. In a binary hypothesis test, there are two event possibilities described by a pair of mutually exclusive hypotheses. The result from the matched filter, x_{MF}, can be assumed to exist in one of two distributions

$$f_0(x) = p_{MF}(x; 0) \tag{12}$$

$$f_1(x; \beta) = p_{MF}(x; \beta), \beta > 0 \tag{13}$$

where the distributions $p_{MF}(x; 0)$ and $p_{MF}(x; \beta)$ are arbitrary probability density functions (PDFs)and have an expected value of 0 and β, respectively.

Eqs. (12)-(13) define the two possible distributions for a matched filter result given an event did or did not occur. The following null and alternate hypotheses are then defined as

$$\mathcal{H}_0 : x \sim f_0(x) \tag{14}$$

$$\mathcal{H}_1 : x \sim f_1(x;\beta); \beta = x_{MF} \tag{15}$$

In the null hypothesis, $\mathcal{H}_0$, the measured data is due to zero-mean magnetometer measurement noise and magnetospheric phenomenon. Otherwise, the alternate (detection) hypothesis, $\mathcal{H}_1$, describes when the measured data is due to both noise and the signal of interest based on a hypothesized charged RSO flyby. Given observations and corresponding PDFs of the hypotheses, $f_0(x)$ and $f_1(x)$, the most likely hypothesis can be computed using the following probabilities:

$$P_{FA} = \int_{\nu}^{\infty} f_0(x)dx \tag{16}$$

$$P_{FN} = \int_{-\infty}^{\nu} f_1(x)dx \tag{17}$$

$$P_D = \int_{\nu}^{\infty} f_1(x)dx \tag{18}$$

where ν is a selected threshold, P_{FA} is the probability of false alarm, P_{FN} is the probability of false negative, and P_D is the probability of detection [22]. The threshold ν is generally set to meet a maximum false alarm rate using the null hypothesis PDF and Eq. (16).

Eq. (16)-(18) describe a one-sided hypothesis test given the null and detection hypotheses. Using a one-sided hypothesis test determines whether the expected value of the detection hypothesis PDF, β, is sufficiently greater than the expected value of the null hypothesis PDF, 0. In the event that a large deviation in the magnetic field has occurred, the detection hypothesis PDF would be shifted far from the null hypothesis PDF. Using a small P_{FA} and corresponding ν, the detection probability P_D would be large, indicating that a detection has likely occurred. Fig. 8 provides a depiction of the computation of these probabilities from the $\mathcal{H}_0$ and $\mathcal{H}_1$ PDFs.

It is assumed for this work that the PDFs for the null and detection hypotheses are Gaussian. As a result, the binary hypothesis test defined by

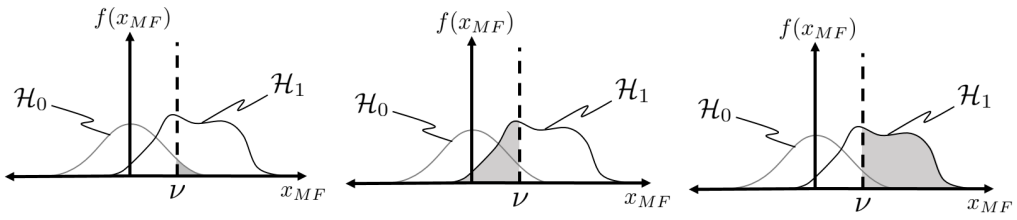

(a) P_{FA} (b) P_{FN} (c) P_D

Figure 8: Two-sided binary hypothesis testing illustration

Eq. (16)-(18) have closed form solutions given the mean and variance of the null and detection hypothesis PDFs. For the null and detection hypotheses, the matched filter result is primarily driven by the zero-mean measurement noise of the magnetometer with specified variance σ_w^2.

Given a candidate matched filter detection, $SNR_{\text{MF}} > SNR_{\text{thresh}}$, a binary hypothesis test can be conducted to probabilistically identify whether the detection was a false positive. As a result of the scoring process, the candidate detection is characterized by a RSO flyby signature of rate ω_h and closest approach time of t_c. As described in Eq. (10), the duration of the flyby is characterized by Δt. In the discrete domain, this interval is defined as

$$\mathcal{D} \triangleq \{t_i \mid t_c - \tfrac{\Delta t}{2} \leq t_i \leq t_c + \tfrac{\Delta t}{2}, i \in \mathcal{S}\} \tag{19}$$

where $\mathcal{S}$: set of measurement times. The null hypothesis PDF is generated from

$$\mathcal{H}_0 : x \sim \mathcal{N}(0,\, \sigma_w^2(t_c)) \tag{20}$$

where $\sigma_w^2(t_c)$ corresponds to the variance of the magnetometer measurements at the hypothesized RSO flyby closest approach time. To compute the alternate hypothesis PDF, Eqs. (21)-(24) are used to describe the mean and variance of a hypothesized RSO flyby signal.

$$\|\mathbf{B}(t_i)\| = B_i = s_i + w_i, \mathbb{E}[w_i] = 0 \tag{21}$$

$$x_{MF} = \sum_{i \in \mathcal{D}} B_i g_i = \sum_{i \in \mathcal{D}} (s_i + w_i) g_i \tag{22}$$

$$\mathbb{E}[x_{MF}] = \sum_{i \in \mathcal{D}} \mathbb{E}[B_i] g_i = \sum_{i \in \mathcal{D}} s_i g_i \tag{23}$$

$$\mathrm{Var}[x_{MF}] = \mathbb{E}\left[\left(\sum_{i\in\mathcal{D}} B_i g_i\right)^2\right] = \sigma_w^2 \sum_{i\in\mathcal{D}} g_i^2 \tag{24}$$

Once the null and detection hypothesis PDFs are constructed, the probability of false alarm P_{FA} is specified. This user-specified rate is generally small (1-20%) to minimize the number of false positives from the BHT procedure. The integration threshold ν is then computed from Eq. (16). Using Eq. (18), the detection probability can be computed. For a detection to be declared, the detection probability should be meet or exceed a user-specified detection probability threshold $P_{D,\text{thresh}}$. This threshold is typically set large (80-99%) to minimize the number of false negatives from the BHT procedure because $P_D + P_{FN} = 1$.

3. Experimental Data and Results

3.1. THEMIS Mission Description

The THEMIS mission, launched in 2007, studies magnetic substorms and the interactions in Earth's magnetosphere that influence them. The constellation maintained five spacecraft until spring 2011 when two of the spacecraft separated into a new NASA mission around the Moon. This new mission, "Acceleration, Reconnection, Turbulence and Electrodynamics of the Moons Interaction with the Sun" (ARTEMIS), measures the effect of the Sun's radiation the Moon [2]. To aid in the characterization of the magnetosphere and magnetic substorms, the THEMIS mission measures the local magnetic field using search-coil and fluxgate magnetometers. As shown in Figure 9(a), the THEMIS spacecraft were placed in highly elliptical orbits where the respective apogee rotate slowly around the Earth to survey the various sections (i.e. day-side, night-side, etc.) of the magnetosphere. After the departure of the two ARTEMIS spacecraft in early 2010, the remaining THEMIS spacecraft settled into a science orbit, displayed in Figure 9(b), to continue monitoring space weather phenomenon.

To accomplish the mission's science goals, the THEMIS spacecraft incorporate high sampling rate on-board fluxgate magnetometers with 3-σ measurement uncertainties of 10 pT/$\sqrt{\text{Hz}}$ at 1 Hz [7]. At the magnetometers maximum sampling rate of 128 Hz, this corresponds to a 3-σ measurement uncertainty of 113 pT, which is on the order or lower than the magnitude of the potential magnetic signature from a RSO.

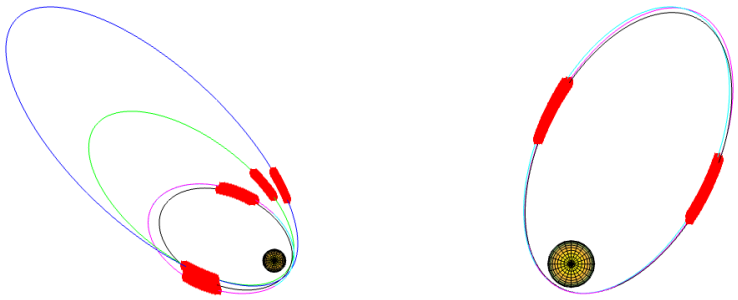

(a) Orbit Geometry 2007-2009 (b) Orbit Geometry 2010-Present

Figure 9: THEMIS orbit diagrams with highlighted GEO altitude belt

To measure the characteristics and behavior of magnetosphere phenomena, the science instruments on each THEMIS craft operate in one of four science collection modes: slow survey, fast survey, particle burst, and wave burst. For the majority of an orbit, the spacecraft operates in slow survey, returning electric, magnetic, and plasma parameters once every 3 seconds (1/3 Hz). Near apogee in the magnetotail and regions of interest like the dayside (towards Sun) magnetopause, the spacecraft operates in fast survey mode, collecting data at 4 Hz. Additionally, encounters with the bow shock, magnetopause, high density plasma regions, geomagnetic storms, and other phenomena trigger burst mode operations, where the fluxgate magnetometer can sample the magnetic field at 128 Hz [7]. Because the magnetometer detection capability increases with sampling rate, only the high-frequency, 128 Hz, data is used.

3.2. Extraction and Processing of Data

In this study, only the altitudes neighboring geostationary orbit (32,000-52,000 km) are of interest, as highlighted in Figure 9. As such, the THEMIS fluxgate magnetometer datasets from only these altitudes are processed in the matched filter scoring process. Due to Debye lengths on the centimeter to meter scale, charge screening severely limits detection ranges to less to 1 m at LEO altitude. At an orbit radius of 32,000 km, the Debye length reaches values at which space object detection using magnetometers is feasible. Orbit radii above 52,000 km are not considered because this study focuses on potential GEO debris.

The NASA Coordinated Data Analysis Web data service and the NASA Space Physics Data Facility provide a publicly-released database directly accessible as an anonymous File Transfer Protocol (FTP) service [1]. In the aforementioned matched filter process, the data volume to access and analyze is large due to the high resolution data products supplied from each of the THEMIS spacecraft. As shown in Figure 10, the total amount of data parsed and analyzed was about 475 GB.

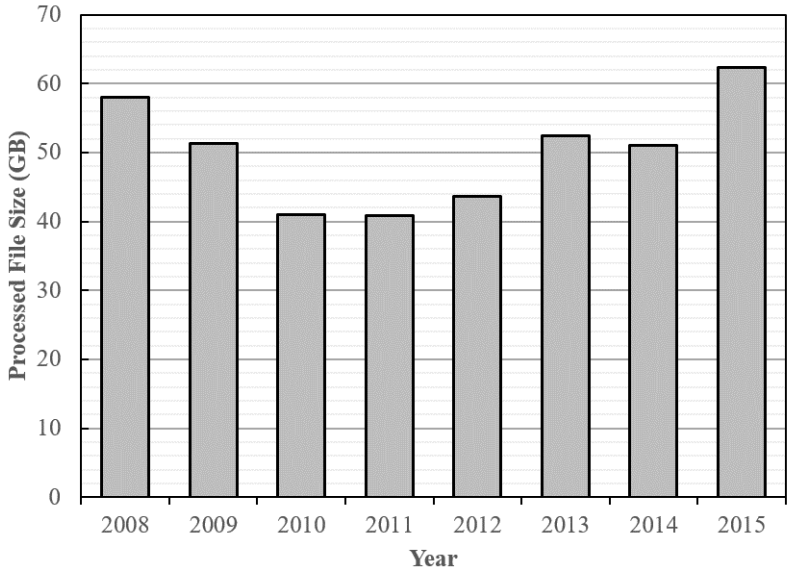

Figure 10: Total THEMIS fluxgate magnetometer data volume processed

The data capacity and computational requirements of this problem called for the use of the Partnership for an Advanced Computing Environment (PACE) high-performing computing clusters at the Georgia Institute of Technology. The PACE clusters are used for the acquisition of the fluxgate magnetometer data, parsing and constraining the data, as well as the computations involved in the matched filter scoring process to detect RSO encounters. Additionally, there are large benefits in computation speed provided by the capability to parallelize the computation processes across multiple nodes of the cluster.

[1] https://cdaweb.sci.gsfc.nasa.gov/index.html

Figure 11 summarizes the overall algorithm used to acquire and process the THEMIS magnetometer data. The first component of the process involves pulling the fluxgate magnetometer data from public NASA servers. Once the magnetometer data is acquired in the form of a Common Data Format (CDF) file, the contents of this archived file are unpacked into the relevant data products such as spacecraft orbital state arrays, state time arrays, high resolution fluxgate magnetometer magnetic field arrays, and its corresponding time arrays.

The magnetometer data that satisfies the orbital constraint is then passed through the matched filter scoring process. This includes the low pass filtering and matched filter conducted at each ω_h of interest. For a given section of data, if any of the local maxima of the SNR scoring surface exceed a set threshold (typically $SNR_{\text{MF}} > 5$), then the output file is appended with the primary parameters describing the signature and matched filter results. These parameters include:

- the THEMIS spacecraft (A-E) that measured the signature of interest
- the Unix time (epoch seconds since January 1, 1970 UTC) of the local maximum of the SNR scoring surface corresponding to the time at which the hypothesized RSO would reach its closest approach distance to the magnetometer (t_c)
- the estimated maximum instantaneous apparent angular rate (ω_h) of the hypothesized RSO flyby
- the score of the matched filter process corresponding to the estimate of the local SNR of the signature of interest

The first two parameters listed are required for retrieval of the state and magnetometer signals while the final two parameters fully describe the estimated magnetic signature due solely to the hypothesized RSO. All of the parameters form the minimal set to represent the magnetic signature of a potential charged RSO encounter.

After the matched filtering scoring process, the candidate detections are then checked for feasible Coulomb charges based on the discussion in Sec. 2.5. If the magnetic signature is feasible in terms of electric charge, a binary hypothesis test is conducted to rigorously test the signal existence hypothesis

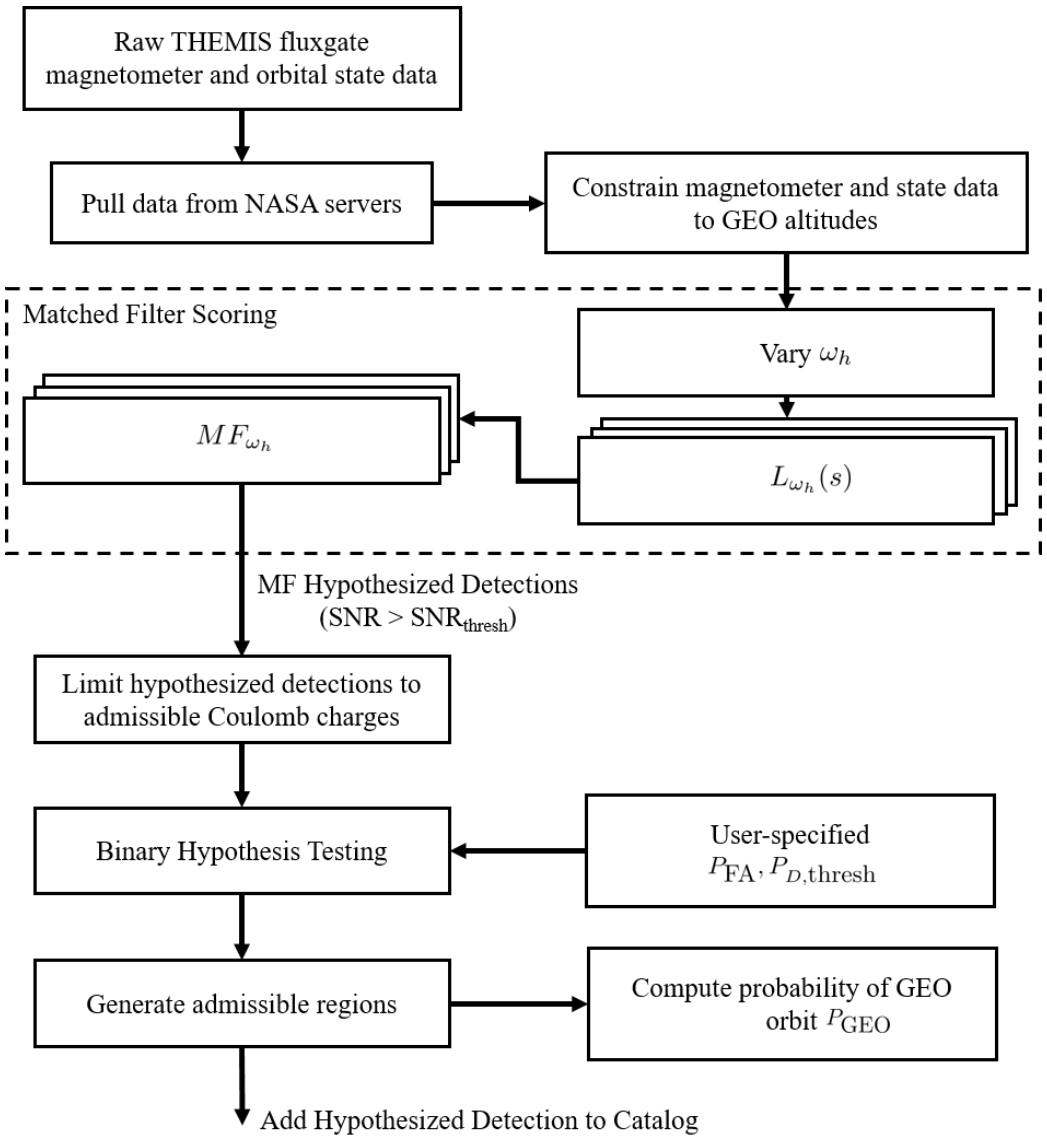

Figure 11: THEMIS data mining process diagram

against evidence contained in the empirical signal. For the results of this paper, the prescribed false alarm rate P_{FA} and detection probability threshold $P_{D,\text{thresh}}$ were chosen to be 10% and 80 %, respectively.

For these candidate detections from the binary hypothesis test, admissible

regions are computed to find the set of orbits that could feasible produce the measured magnetic field signature. Additionally, conducting a uniform Monte Carlo sampling of the admissible region allows for the computation of feasible orbital element parameters. Orbits that are near GEO elements are considered to have a semimajor axis between 32,000 and 52,000 km, orbital eccentricity less than about 0.4, and an inclination below 20 degrees. By dividing the number of Monte Carlo samples that are characterized as near GEO by the number of total Monte Carlo samples, a probability of GEO is formed [16, 15].

Python is used as the programming language for this work due to the built-in and external open-source modules designed for FTP file retrieval and CDF extraction. Python is also advantageous in terms of computation speed and simple terminal interface for use on the GT PACE clusters.

3.3. Results

First, Section 3.3.1 demonstrates the complete archival fluxgate magnetometer data mining process described in Section 3.2 and Figure 11 on one of the hypothesized detections discovered using this approach. Section 3.3.2 then summarizes the cumulative results from this data mining. Finally, Section 3.3.3 discusses the significance and potential factors affecting the overall data mining results.

3.3.1. Example Data Processing

From the analyzed dataset, a particular case of interest is the magnetometer signal from the THEMIS-A spacecraft with a UTC epoch time of 10-Aug-11 12:02:21. This case demonstrates the capability of the matched filter scoring process in detecting magnetic field signatures characteristic of the induced magnetic field signature of a RSO flyby. The following figures detail the scoring process results on this particular dataset.

Following the process diagram outlined in Figure 11, the magnetic background signal is extracted using a fourth order zero phase low pass Butterworth filter with cut-off frequency, ω_h. In the case shown in Figure 12, ω_h = 1.584 rad/s from the scoring process is used as the cut-off frequency of the filter. As a result, the residual is a zero-mean signal that represents fluctuations over the baseline magnetic field. At larger ω_h values of the scoring process, the low pass filter would instead attenuate this peak in the magnetic field magnitude resulting in lower estimates of SNR.

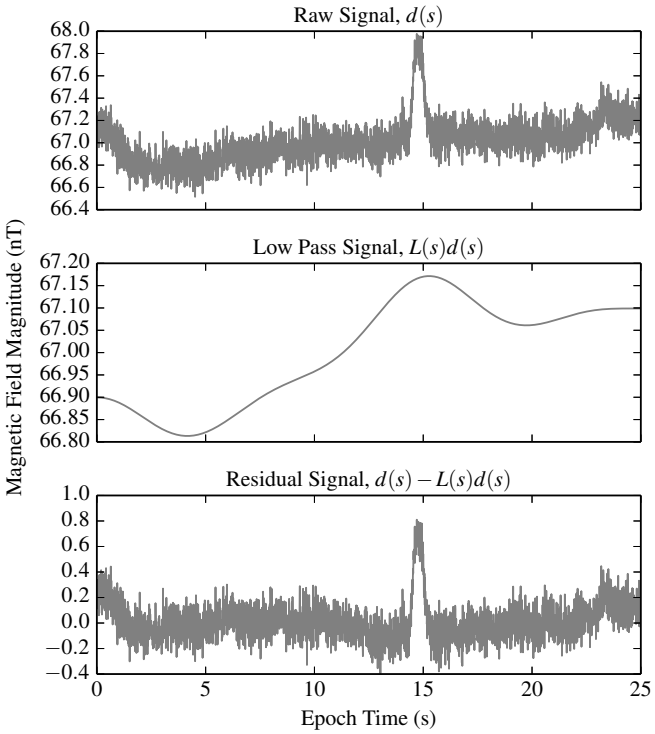

Figure 12: Low pass filter on THEMIS-A dataset (at highest score ω_h=1.584 rad/s)

Next, a sequence of hypotheses are tested at varying ω_h values and times of closest approach using a matched filter. This results in a 3-dimensional scoring surface of SNR estimates with results shown in both Figure 13 and Figure 14. The maximum ω_h and t_c of the peak suggest the maximum likelihood estimate for the RSO flyby. For this particular dataset, the estimated SNR of the signature is approximately 5.67, the estimated angular rate is 1.584 rad/s, and the UTC time of closest approach of 10-Aug-11 12:02:36.

From the estimates generated from the scoring surface maxima, an artificial estimate signal is generated. When this artificial estimate signal is plotted with the true raw magnetometer signal, as in Figure 15.

Visually, and in terms of the estimate parameters, the THEMIS-A dataset being discussed has a signature that is characteristic of a RSO encounter. To

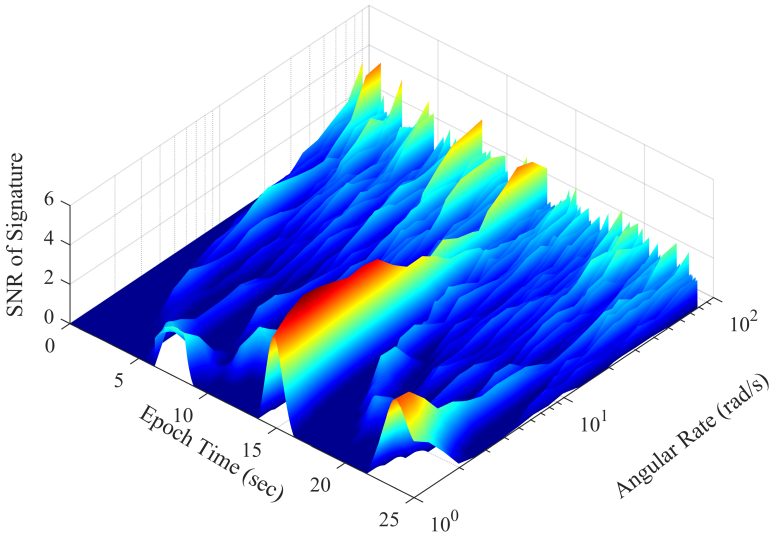

Figure 13: SNR surface for THEMIS-A dataset with a UTC epoch time of 10-Aug-11 12:02:21

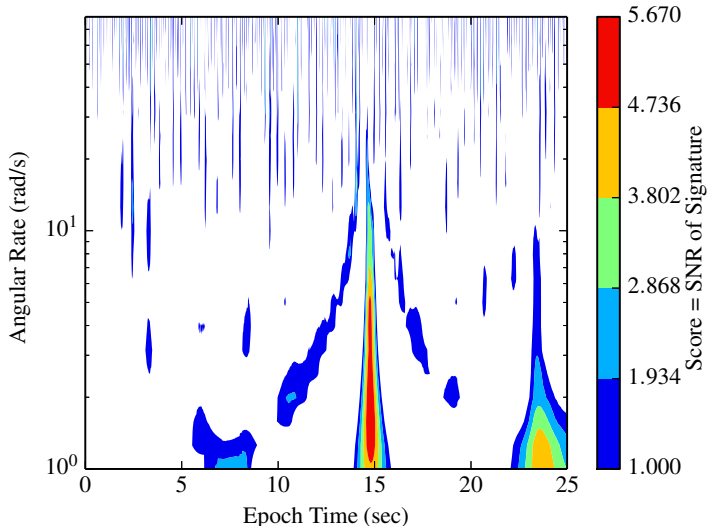

Figure 14: SNR contour for THEMIS-A dataset with a UTC epoch time of 10-Aug-11 12:02:21

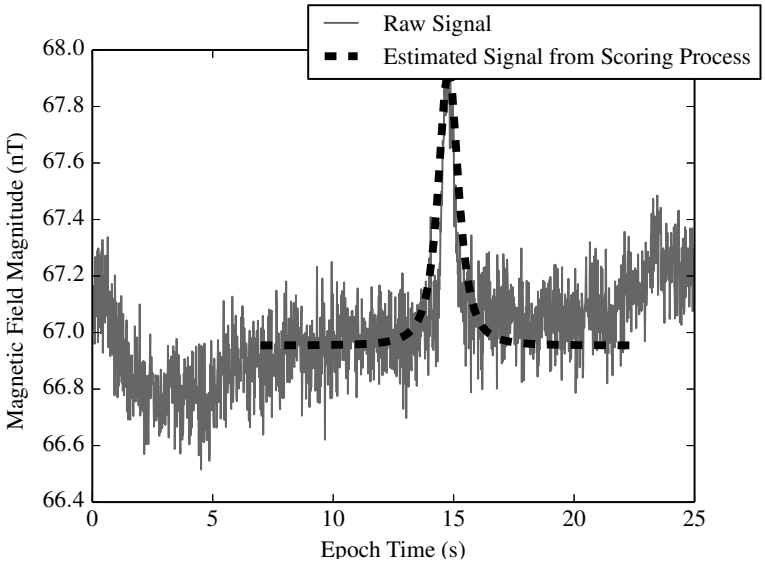

Figure 15: Matched filter estimate over raw THEMIS-A signal with a UTC epoch time of 10-Aug-11 12:02:21

continue to support this hypothesis, an admissible region is formed to further constrain the possible states of the RSO. It is common to constrain detected space objects to have a negative orbital energy - relating to a closed Earth orbit. Holzinger showed the boundary of the admissible region constrained by maximum mass-specific energy may be found by computing the roots of a 7th order polynomial in $\rho_\perp$ [19]. Using this, samples of the admissible closed orbits are plotted as shown in Figure 16. Figure 17 shows how the orbit solution space reduces when the solution set is limited to the GEO semi-major axis, eccentricity, and inclination bounds identified above.

Both the detection and elliptical orbit constraints are plotted in Figure 18. In this figure the light gray regions satisfy one of the constraints and the darker region, the joint admissible region, satisfies all constraints. For this particular case, the closed orbit constraint volume completely encompasses the detection constraint volume; the joint constraint volume may then be reduced to the detection constraint volume.

Figure 19-20 summarize the scoring results for 2 additional plausible RSO flybys.

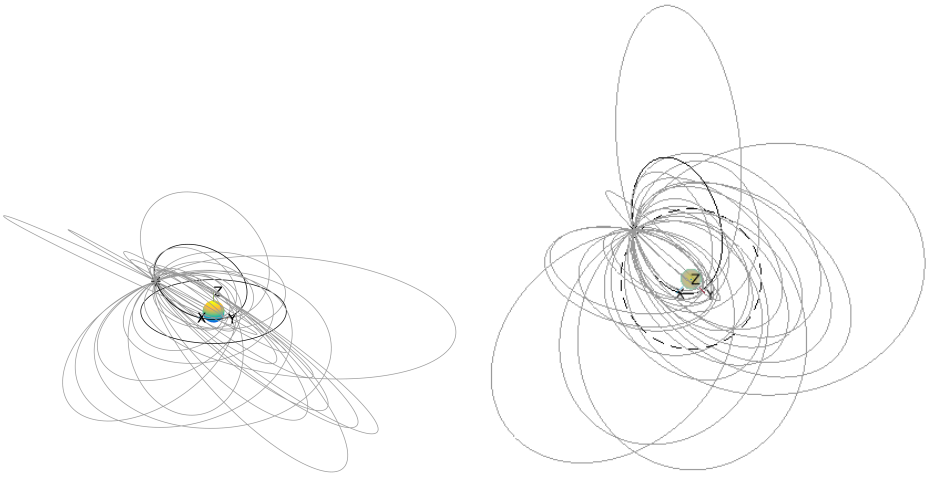

(a) Isometric View (b) Top View ($\hat{\mathbf{i}} - \hat{\mathbf{j}}$ plane)

Figure 16: Closed orbit solutions to admissible region for THEMIS-A dataset with a UTC epoch time of 10-Aug-11 12:02:21

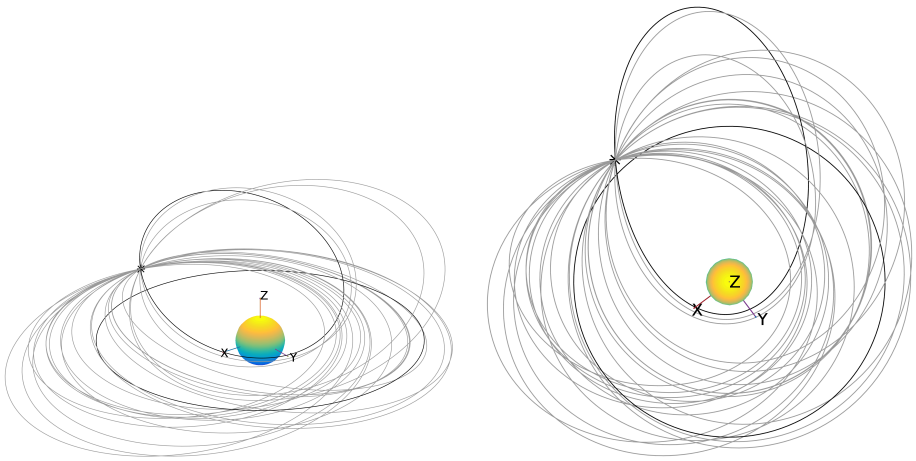

(a) Isometric View (b) Top View ($\hat{\mathbf{i}} - \hat{\mathbf{j}}$ plane)

Figure 17: GEO altitude orbit solutions to admissible region for THEMIS-A dataset with a UTC epoch time of 10-Aug-11 12:02:21

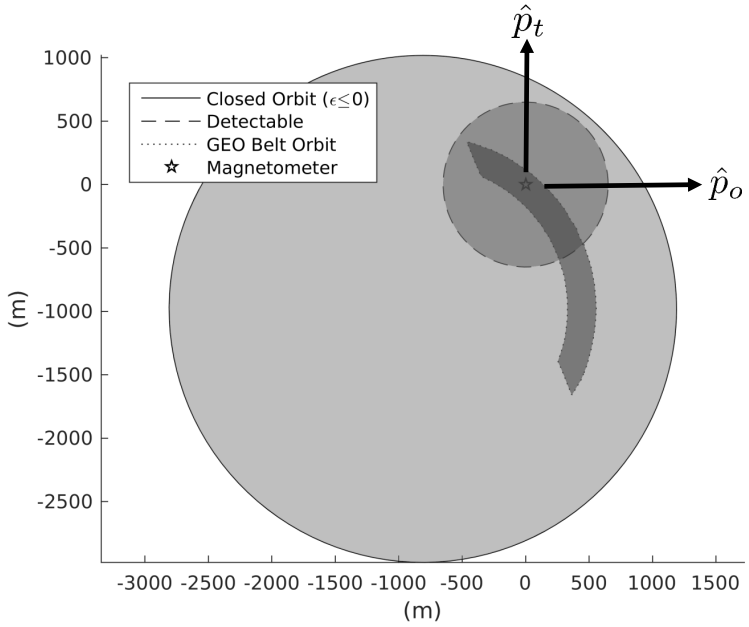

Figure 18: Admissible region constraints in encounter plane for THEMIS-A dataset with a UTC epoch time of 10-Aug-11 12:02:21

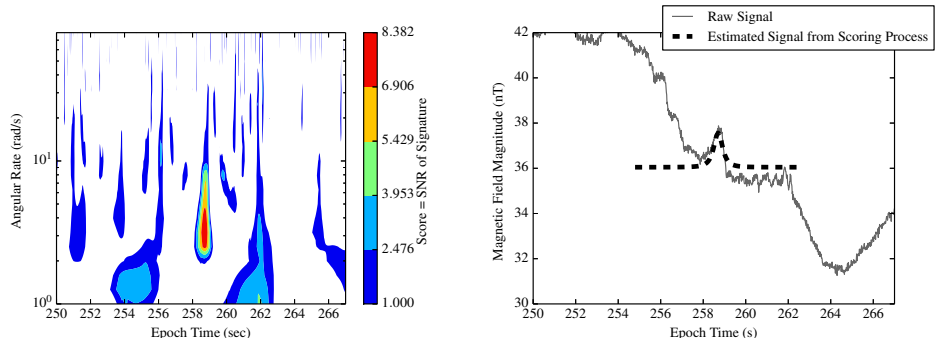

(a) Scoring Contour (SNR Estimate = 8.391)

(b) Estimate Signal Overlay (ω_m Estimate = 3.158 rad/s)

Figure 19: THEMIS-E scoring algorithm results from UTC epoch time on Monday, 10-May-10 13:24:57

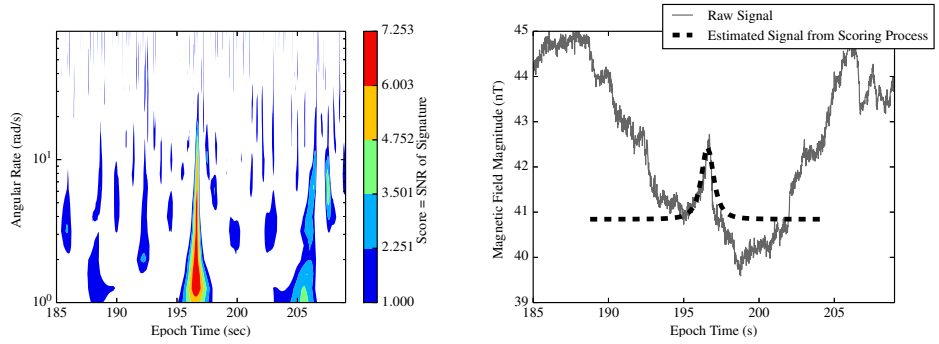

(a) Scoring Contour (SNR Estimate = 7.258)

(b) Estimate Signal Overlay (ω_m Estimate = 1.584 rad/s)

Figure 20: THEMIS-D scoring algorithm results from UTC epoch time on Monday, 10-May-10 13:30:00

3.3.2. Overall Detection Search Results

The results of the matched filter portion of the data mining process are shown in Table 1. After all of the data processing outlined above to identify plausible RSO detections, the total number of hypothesized detections over the specified time period was 288. For each THEMIS spacecraft, this table lists the number of magnetic signatures that are characteristic of charged RSO encounters.

Table 1: Matched Filter Detection Count - MF Estimate SNR > 3

THEMIS S/C	A	B	C	D	E	Annual Total
2008	13	2	4	16	5	40
2009	6	0	2	14	6	28
2010	13	-	-	38	15	66
2011	15	-	-	33	8	56
2012	29	-	-	35	33	97
2013	0	-	-	71	74	145
2014	0	-	-	63	69	132
2015	0	-	-	38	28	66
Craft Total	76	2	6	308	238	**630**

In early 2010, THEMIS-B and THEMIS-C branched into the ARTEMIS mission. From this point, the fluxgate magnetometer data was neglected from these spacecraft for this paper as the spacecraft are outside of the specified GEO altitude range. Over the primary years of the THEMIS mission, there were very few plausible detections from these two spacecraft. This is attributed to the high apoapses of THEMIS-B and THEMIS-C, about 190,000 and 128,000 km respectively. Due to the large semi-major axis, these spacecraft spend a relatively small amount of time within the GEO altitude range of interest.

Alternatively, the A, D, and E THEMIS spacecraft maintained lower apogee ranging from about 64,000 to 83,000 km. These spacecraft spend more time in or near GEO altitudes and have a higher probability of encountering a RSO.

Figure 21 displays the hypothesized detections and the cataloged RSOs in the specified GEO search region plotted in the Earth-centered Earth-Fixed (ECEF) reference frame. This reference frame rotates with the Earth about its spin axis so geosynchronous satellites maintain fixed longitudinally. Collections of hypothesized detections near geostationary satellites are visible. It should also be noted that there are a number of hypothesized detections at non-zero latitudes, corresponding to possibilities of charged GEO graveyard orbit RSO flybys.

Figure 22 shows how the overall hypothesized detection count varies solely with the maximum allowable false alarm rate P_{FA} and the probability of detection threshold $P_{D,\text{thresh}}$ in the BHT process. As displayed in Fig. 22, the threshold for the probability of detection is the primary factor in the

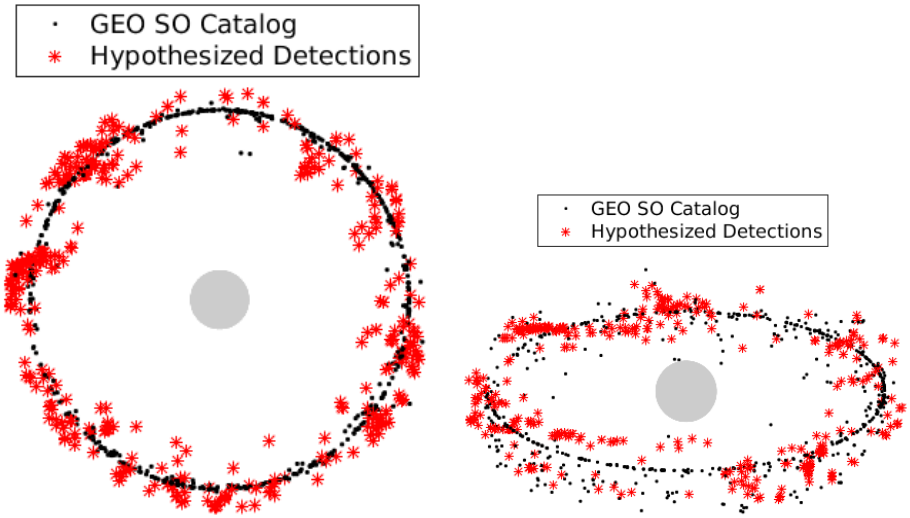

(a) Top-Down View (b) Isometric View

Figure 21: Hypothesized Detections Overlay on GEO Belt in Earth-Centered Earth-Fixed (ECEF) frame

number of overall hypothesized detections using the discussed matched filter and binary hypothesis test approach. In general, these parameters are user-specified and are chosen to allow for more false positives while minimizing false negatives.

For a complete catalog of the hypothesized detections using the discussed methodology and parameters, refer to **??**.

3.3.3. Discussion of Results

It is necessary to place the catalog of detections contained within **??** in context of space weather. To do so, the effective detection rate of THEMIS satellites while in the selected altitudes is computed and compared to various space weather phenomena, as well as annual orientation changes in the magnetosphere. Finally, to address the hypothesis that the plausible detections may result from shed RSO debris, an analysis is performed to investigate the consistency between GEO orbits and plausible detected RSO orbits.

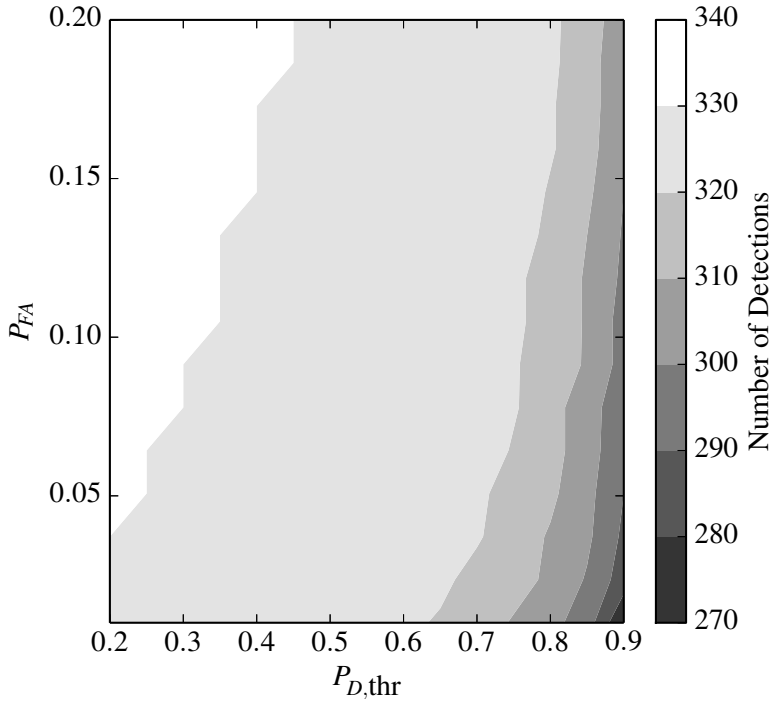

Figure 22: Number of BHT detections with varying P_{FA} and $P_{D,\text{thresh}}$

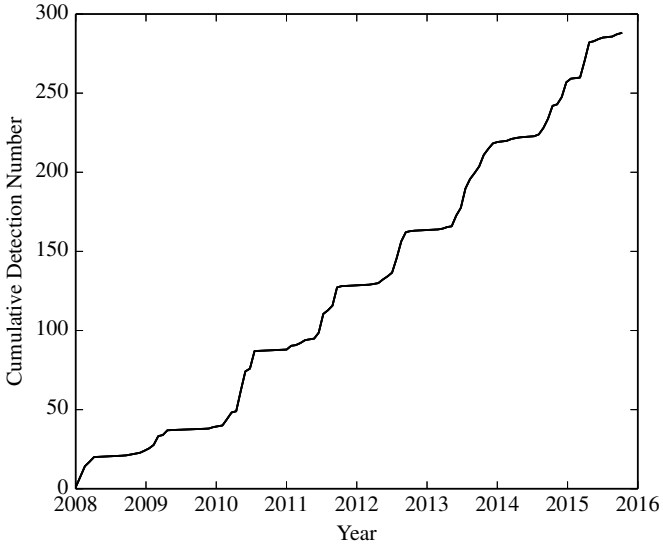

(a) Cumulative Detection Count over Time

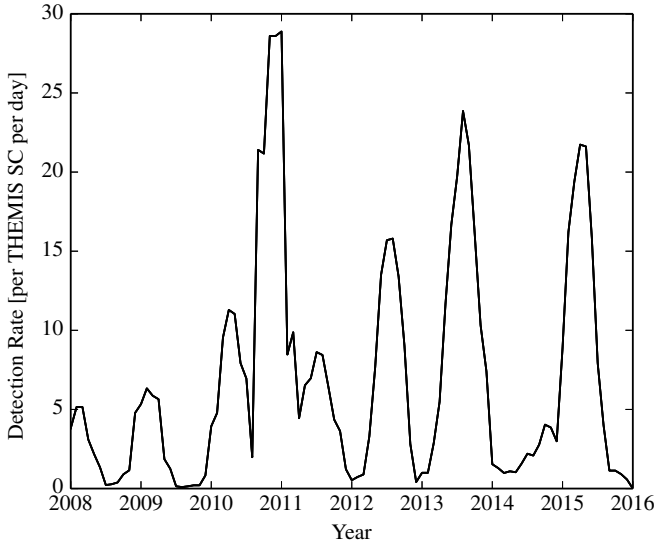

(b) Detection rate for a fluxgate magnetometer per day within the extended GEO belt

Figure 23: Hypothesized Detection Count and S/C normalized Detection Rate

Figure 23 shows how the hypothesized detections were distributed in time. As previously mentioned in Section 3.1, the high frequency (128 Hz) fluxgate magnetometer data was collected during short time intervals. As a result, the time spent measuring high-frequency magnetometer data in the specified GEO search region is a small fraction of the spacecraft's total orbital time in the GEO region. For example, the total high-frequency measurement duration for all of the THEMIS spacecraft is about 0.5% of the total orbital time.

To account for this, the high-frequency measurement durations are summed for each THEMIS spacecraft into monthly bins. For each of these months, the total of hypothesized detections are counted. Then the monthly effective detection rate is computed by dividing the number of new hypothesized detections by the measurement durations for that month. By also normalizing by the number of active THEMIS spacecraft, the THEMIS constellation monthly effective detection rate is computed. These quantities plotted in Figure 23(b) correspond to the estimated number of detections per THEMIS spacecraft during one full day of high-frequency the fluxgate magnetometer data collection. This definition of constellation detection rate is used for the remainder of the paper.

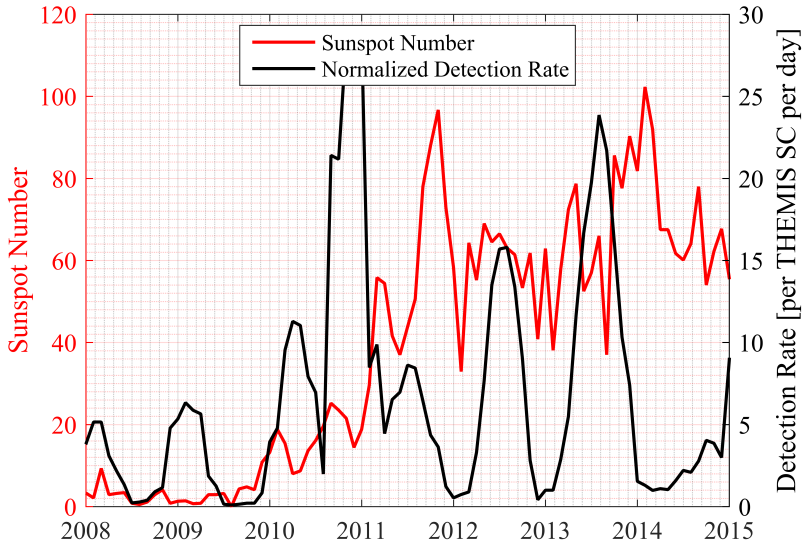

Figure 24: Detection Rate Correlation with Sunspot Number

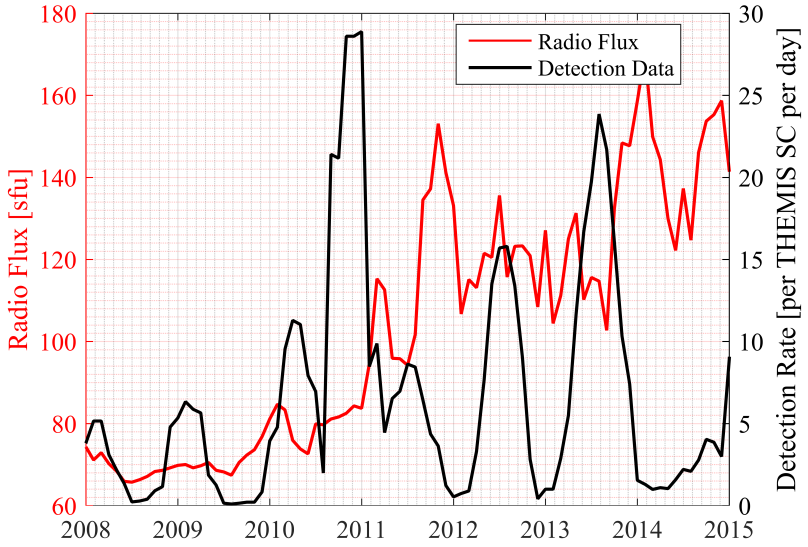

Figure 25: Detection Correlation with Radio Flux

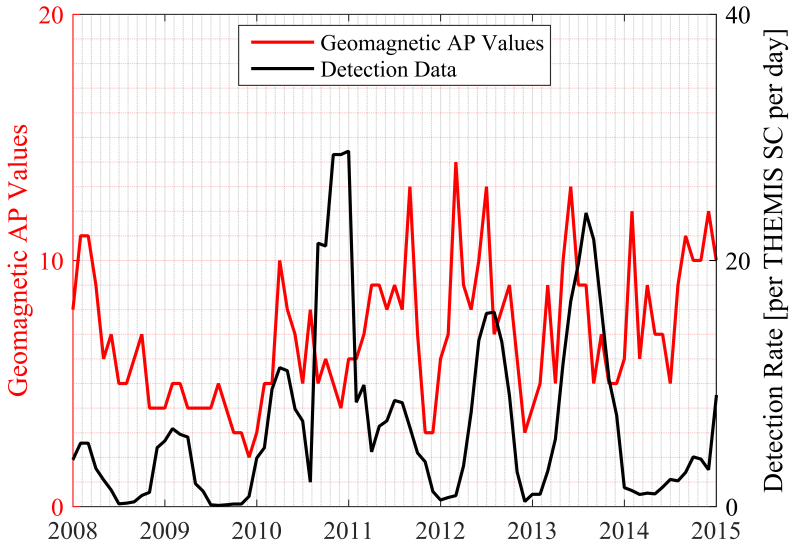

Figure 26: Detection Correlation with Geomagnetic AP Values

Figure 23(b) displays a clear quasi-annual trend in the detection rate. There is also a general upward trend in the peak detection rates over time. One of the primary causes of these trends are hypothesized to be the solar and geomagnetic activity during the high-frequency measurement durations. Figures 24-26 compare the detection rate with various solar cycle indices such as sunspot number, radio flux, and geomagnetic AP values. This data is retrieved from the NOAA Space Weather Prediction Center [1]. These plots suggest a correlation between the hypothesized detection rate of the RSOs and solar activity. This is to be expected because high levels of solar activity result in larger Debye lengths and increased spacecraft charging. As aforementioned, large Debye lengths also result in an enhanced capability to detect charged RSOs using a magnetometer [19, 8].

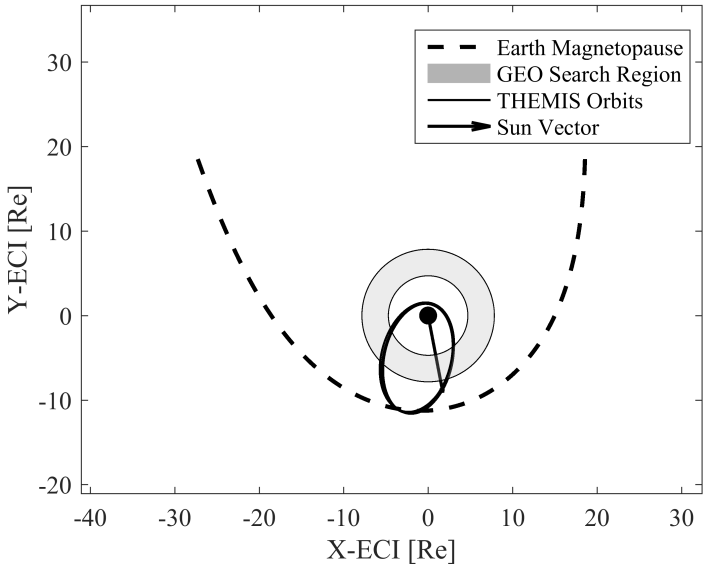

Figure 27: THEMIS and Solar Orbital Geometry on UTC time 01-Jan-2012 00:00:00

THEMIS orbital geometry also plays an important role in the detection rate. Observing the year 2012 in 23(b), January corresponds to a local minimum in detection rate while July corresponds to a local maximum. Figures 27 - 28 display the orbital geometry of THEMIS A, D, and E spacecraft at

[1] http://www.swpc.noaa.gov/products/solar-cycle-progression

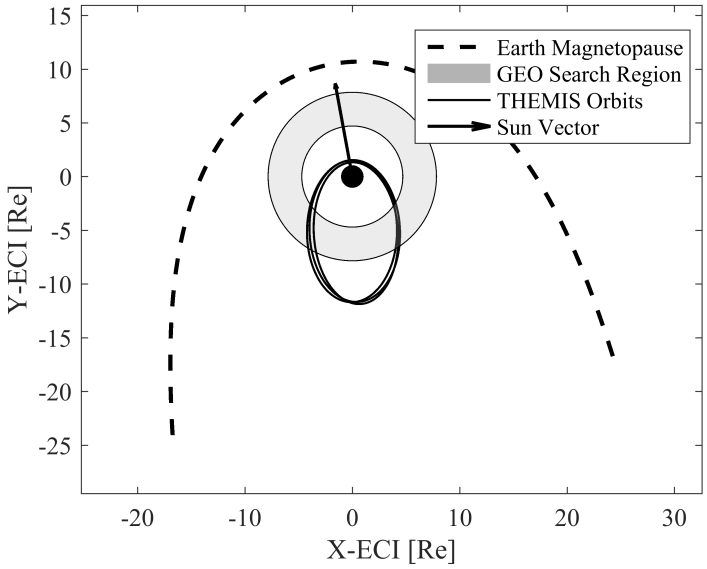

Figure 28: THEMIS and Solar Orbital Geometry on UTC time 01-Jul-2012 00:00:00

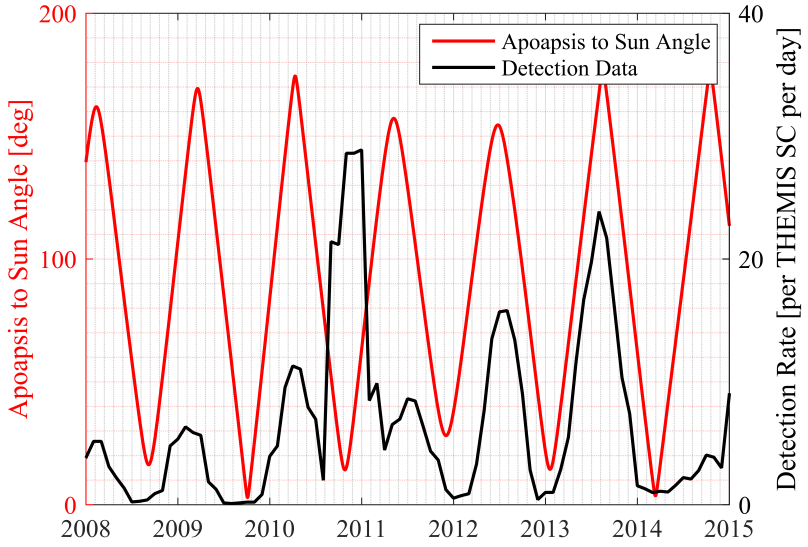

Figure 29: Detection Rate correlation with angle between THEMIS orbit apoapsis and sun vector

these two times in the Earth-centered inertial (ECI) reference frame. It can be seen that when the apoapsis vector is closely aligned with the sun vector, the detection rate decreases and vice-versa. This periodic trend can be visualized over all the years of interest in Figure 29.

These results show that the detection rate of the THEMIS constellation is primarily driven by the orbital geometry and space weather conditions. The cause of the large peak in the detection rate near the year 2011 is unknown. This can be attributed to a number of causes such as a geomagnetic storm or collection of charged RSO flybys from a GEO-altitude defragmentation.

For each hypothesized detection, an admissible region can be formed that represents the possible magnetometer flyby trajectories that result in a closed orbit. These admissible regions can then be uniformly sampled to determine the distribution of possible closed orbits. By taking hypothesis orbits drawn from the admissible region, a mapping into orbital element space can be performed. Admissible regions are uninformative priors so care must taken if these samples used as a prior for an estimator [15]. However, these Monte Carlo samples lead to interesting insight into the relative densities of admissible orbits in orbital element space. Figure 30 shows the mappings of the Monte Carlo samplings to orbital element space. As shown in these figures, there is a significant overlap between the admissible regions and GEO-like orbital solutions, highlighted in gray. Allan and Cook have shown that geosynchronous satellites will have periodic inclination variations of 0-15° due to earth oblateness and lunar-solar gravitational forces [1]. This high density of closed orbit inclination solutions within this oscillation band suggests that a number of geosynchronous satellites lie within the admissible regions of the hypothesized detections.

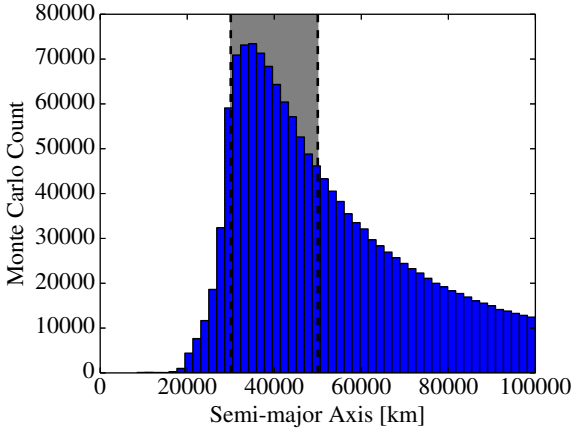

(a) Semimajor Axis Histogram

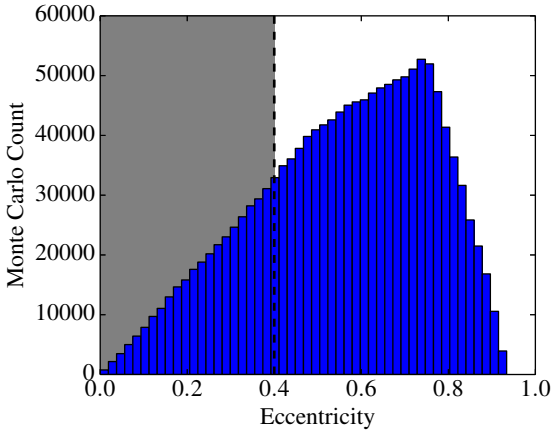

(b) Eccentricity Histogram

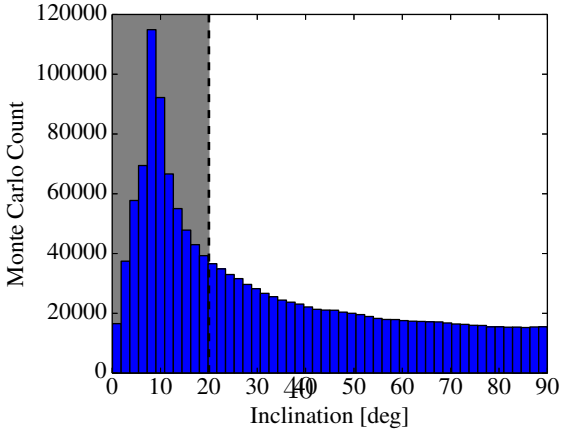

(c) Inclination Histogram

Figure 30: Orbital element histograms from Monte-Carlo sampling of admissible regions of all hypothesized detections with GEO-like solutions highlighted

4. Conclusions

In this paper, another phenomenology to detect RSOs at GEO altitudes is investigated. Starting from first principles, matched filtering techniques and signal processing are used to examine the feasibility of using magnetometers to detect RSOs. The matched filter template is proposed and is consistent with the Biot Savart Law and approximate flyby dynamics. The detection capability of the THEMIS fluxgate magnetometers are discussed. To isolate local fluctuations in the baseline magnetic field, filtering and other signal conditioning options for raw magnetometer signals are introduced. The matched filter scoring process is presented and the results provide evidence of magnetic signatures that are characteristic of RSO flybys. Additional constraints are imposed on the signatures of interest using admissible regions and the presented plausible ranges of parameters that describe the signature. Processing of archival THEMIS data generated 285 plausible detections of RSOs within GEO orbits. The detection rate is found to vary with the magnetosphere / THEMIS orbit geometry and space weather. Monte Carlo samples of orbits consistent with the plausible RSO detections suggest a possible connection to known long-term drifts in GEO orbits. More work is needed to 1) corroborate plausible detections using other phenomenologies and 2) to estimate local Debye lengths during encounters, allowing better orbit estimates of plausible detections and to potentially enable follow-up observations.

Acknowledgements

This work was supported by the Georgia Tech Presidents Undergraduate Research Award and NASA Space Technology Research Fellowship Grant No. NNX16AM39H. The views and opinions expressed are those of the authors and do not represent the views of funding agencies.

References

[1] Allan, R. R., Cook, G. E., 1964. The Long-Period Motion of the Plane of a Distant Circular Orbit. Proceedings of the Royal Society of London. Series A, Mathematical and Physical Sciences 280 (1380), 97–109. doi: http://www.jstor.org/stable/2414875

[2] Angelopoulos, V., 2011. The ARTEMIS Mission. Space Science Reviews 165 (1-4), 3–25. doi: http://dx.doi.org/10.1007/s11214-010-9687-2

[3] Anonymous, June 2010. National Space Policy of the United States of America. Tech. rep.

[4] Anonymous, Sep 2012. Continuing Kepler's Quest: Assessing Air Force Space Command's Astrodynamics Standards. The National Academies Press, Washington, DC.
doi: http://dx.doi.org/10.17226/13456

[5] Anz-Meador, P., May 2017. Orbital Debris Quarterly News: The OD Environment in Numbers, nASA Orbital Debris Program Office.
doi: https://www.orbitaldebris.jsc.nasa.gov/quarterly-news/pdfs/odqnv21i2.pdf

[6] Auster, H., Glassmeier, K., et al., 2009. The THEMIS Fluxgate Magnetometer. In: Burch, J., Angelopoulos, V. (Eds.), The THEMIS Mission. Springer New York, pp. 235–264.

[7] Burch, J. L., Angelopoulos, V., 2009. The THEMIS Mission.
doi: http://dx.doi.org/10.1007/978-0-387-89820-9

[8] C. Frueh, D. Ferguson, C. L. M. J., 2014. Passive Electrostatic Charging of Near-Geosynchronous Space Debris HAMR Objects and its Effects on the Coupled Object Dynamics. In: AAS/AIAA Spaceflight Mechanics Meeting.

[9] Choi, H.-S., Lee, J., Cho, K.-S., et al., 2011. Analysis of GEO spacecraft anomalies: Space weather relationships. Space Weather 9 (6), s06001.
doi: http://dx.doi.org/10.1029/2010SW000597

[10] Chulliat, A., Macmillan, S., Alken, P., et al., 2015. The US/UK World Magnetic Model for 2015-2020. Tech. rep.
doi: http://dx.doi.org/10.7289/V5TB14V7

[11] Corless, R. M., Gonnet, G. H., Hare, D. E. G., et al., 1996. On the Lambert W Function. In: Advances in Computational Mathemetics. pp. 329–359.

[12] Cowardin, H., Seitzer, P., Abercromby, K., et al., 2013. Observations of Titan IIIC Transtage Fragmentation Debris. In: Advanced Maui Optical and Space Surveillance Technologies (AMOS) Conference.

[13] Derrick, T., Bates, B., Dufek, J., July 1994. Evaluation of time-series data sets using the Pearson product-moment correlation coefficient. Medicine and science in sports and exercise 26 (7), 919–928.
doi: http://europepmc.org/abstract/MED/7934769

[14] Früh, C., Schildknecht, T., nov 2011. Variation of the area-to-mass ratio of high area-to-mass ratio space debris objects. Monthly Notices of the Royal Astronomical Society 419 (4), 3521–3528.
doi: https://doi.org/10.1111/j.1365-2966.2011.19990.x

[15] Fujimoto, K., Scheeres, D. J., aug 2013. Applications of the admissible region to space-based observations. Advances in Space Research 52 (4), 696–704.
doi: https://doi.org/10.1016%2Fj.asr.2013.04.020

[16] Fujimoto, K., Scheeres, D. J., Herzog, J., Schildknecht, T., 2014. Association of optical tracklets from a geosynchronous belt survey via the direct Bayesian admissible region approach. Advances in Space Research 53 (2), 295 – 308.
doi: http://www.sciencedirect.com/science/article/pii/S0273117713007059

[17] Glaßmeier, K. H., 2007. Geomagnetic pulsations. Springer Netherlands, Dordrecht, pp. 333–334.
doi: http://dx.doi.org/10.1007/978-1-4020-4423-6_122

[18] Gural, P. S., Larsen, J. A., Gleason, A. E., 2005. Matched Filter Processing for Asteroid Detection. The Astronomical Journal 130 (4), 1951.
doi: http://stacks.iop.org/1538-3881/130/i=4/a=1951

[19] Holzinger, M. J., Sep 2014. Using Magnetometers for Space Object Characterization in Space Situational Awareness Applications. Journal of Guidance, Control, and Dynamics 37 (5), 1397–1405.
doi: http://dx.doi.org/10.2514/1.G000523

[20] Johnson, N., Gabbard, J., DeVere, G., Johnson, E., 1984. History of On-Orbit Satellite Fragmentations, 1st Edition. Teledyne Brown Engineering, Colorado Springs, Colorado 80910.

[21] Kinard, W., Armstrong, D., Crockett, S., Jones, J., Kassel, P., Wortman, J., Feb 1995. Orbiting Meteoroid and Debris Counting Experiment.

In: LDEF: 69 Months in Space. Third Post-Retrieval Symposium. Vol. 1 of LDEF (Long Duration Exposure Facility): 69 Months in Space. Third Post-Retrieval Symposium. NASA Langley Research Center, Hampton, VA.

[22] Lehmann, E., Romano, J., 2005. Testing Statistical Hypotheses, 3rd Edition. Springer Texts in Statistics. Springer-Verlag New York.

[23] Makovec, K. L., 2001. A Nonlinear Magnetic Controller for Three-Axis Stability of Nanosatellites. Ph.D. thesis, Virginia Polytechnic Institute and State University.

[24] Milani, A., Gronchi, G. F., Vitturi, M. D. M., Knežević, Z., 2004. Orbit determination with very short arcs. I admissible regions. Celestial Mechanics and Dynamical Astronomy 90 (1), 57–85.
doi: http://dx.doi.org/10.1007/s10569-004-6593-5

[25] Montgomery, D. C., Runger, G. C., 2010. Applied Statistics and Probability for Engineers, 5th Edition. John Wiley & Sons.

[26] of Science, O., Technology Policy, E. O. o. t. P., November 1995. Interagency report on orbital debris. Tech. rep., The National Science and Technology Council Committee on Transportation Research and Development.

[27] Papi, F., Vo, B. T., Bocquel, M., Vo, B. N., Nov 2013. Multi-target Track-Before-Detect using labeled random finite set. In: 2013 International Conference on Control, Automation and Information Sciences (ICCAIS). pp. 116–121.

[28] Ratcliffe, J. A., 1972. An Introduction to the Ionosphere and Magnetosphere. CUP Archive.

[29] Schildknecht, T., Früh, C., Hinze, A., Herzog, J., 2010. Dynamical Properties of High Area to Mass Ratio Objects in GEO-like Orbits. In: 38th COSPAR Scientific Assembly. Vol. 38 of COSPAR Meeting. p. 5.

[30] Schildknecht, T., Musci, R., et al., April 2005. Optical Observations of Space Debris in High-Altitude Orbits. In: Danesy, D. (Ed.), Proceedings of the 4th European Conference on Space Debris (ESA SP-587). p. 113.

[31] Seubert, C. R., Stiles, L. A., Schaub, H., 2014. Effective Coulomb force modeling for spacecraft in Earth orbit plasmas. Advances in Space Research 54 (2), 209 – 220.
doi: http://www.sciencedirect.com/science/article/pii/S0273117714002191

[32] Sorrentino, G. B. . R., June 2007. Electonic Filter Simulation & Design, 1st Edition. McGraw-Hill Professional.

[33] Thébault, E., Finlay, C. C., Beggan, C. D., et al., 2015. International Geomagnetic Reference Field: the 12th generation. Earth, Planets and Space 67 (1), 79.
doi: http://dx.doi.org/10.1186/s40623-015-0228-9

[34] Thide, B., 2004. Electromagnetic Field Theory, 2nd Edition. Upsilon Books, Uppsala, Sweden.

[35] Tommei, G., Milani, A., Rossi, A., 2007. Orbit determination of space debris: admissible regions. Celestial Mechanics and Dynamical Astronomy 97 (4), 289–304.
doi: http://dx.doi.org/10.1007/s10569-007-9065-x

[36] Townes, S., Israel, D., et al., July 2015. NASA Technology Roadmaps TA 5: Communications, Navigation, and Orbital Debris Tracking and Characterization Systems. Tech. rep.
doi: http://www.nasa.gov/sites/default/files/atoms/files/2015_nasa_technology_roadmaps_ta_5_communication_and_navigation_final.pdf

[37] Turint, G. L., 1960. An introduction to matched filters.

[38] Wang, C., Liu, J. B., Huang, Z. H., et al., dec 2007. Response of the magnetic field in the geosynchronous orbit to solar wind dynamic pressure pulses. Journal of Geophysical Research 112 (A12).
doi: http://dx.doi.org/10.1029/2007JA012664

[39] Zhang, H., Zong, Q.-G., Sibeck, D. G., et al., jan 2009. Dynamic motion of the bow shock and the magnetopause observed by THEMIS spacecraft. Journal of Geophysical Research: Space Physics 114 (A1), n/a–n/a.
doi: http://dx.doi.org/10.1029/2008JA013488